

Open Research Online

The Open University's repository of research publications and other research outputs

Global geologic map of asteroid (101955) Bennu indicates heterogeneous resurfacing in the past 500,000 years

Journal Item

How to cite:

Jawin, E.R.; McCoy, T.J.; Walsh, K.J.; Connolly, H.C.; Ballouz, R.-L.; Ryan, A.J.; Kaplan, H.H.; Pajola, M.; Hamilton, V.E.; Barnouin, O.S.; Emery, J.P.; Rozitis, B.; DellaGiustina, D.N.; Daly, M.G.; Bennett, C.A.; Golish, D.R.; Perry, M.E.; Daly, R.T.; Bierhaus, E.B.; Nolan, M.C.; Enos, H.L. and Lauretta, D.S. (2022). Global geologic map of asteroid (101955) Bennu indicates heterogeneous resurfacing in the past 500,000 years. *Icarus* (Early Access).

For guidance on citations see [FAQs](#).

© 2022 The Authors



<https://creativecommons.org/licenses/by-nc-nd/4.0/>

Version: Accepted Manuscript

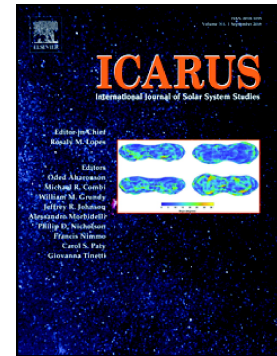
Link(s) to article on publisher's website:

<http://dx.doi.org/doi:10.1016/j.icarus.2022.114992>

Copyright and Moral Rights for the articles on this site are retained by the individual authors and/or other copyright owners. For more information on Open Research Online's data [policy](#) on reuse of materials please consult the policies page.

Global geologic map of asteroid (101955) Benu indicates heterogeneous resurfacing in the past 500,000 years

E.R. Jawin, T.J. McCoy, K.J. Walsh, H.C. Connolly, R.-L. Ballouz, A.J. Ryan, H.H. Kaplan, M. Pajola, V.E. Hamilton, O.S. Barnouin, J.P. Emery, B. Rozitis, D.N. DellaGiustina, M.G. Daly, C.A. Bennett, D.R. Golish, M.E. Perry, R.T. Daly, E.B. Bierhaus, M.C. Nolan, H.L. Enos, D.S. Lauretta



PII: S0019-1035(22)00109-9

DOI: <https://doi.org/10.1016/j.icarus.2022.114992>

Reference: YICAR 114992

To appear in: *Icarus*

Received date: 28 June 2021

Revised date: 8 March 2022

Accepted date: 8 March 2022

Please cite this article as: E.R. Jawin, T.J. McCoy, K.J. Walsh, et al., Global geologic map of asteroid (101955) Benu indicates heterogeneous resurfacing in the past 500,000 years, *Icarus* (2021), <https://doi.org/10.1016/j.icarus.2022.114992>

This is a PDF file of an article that has undergone enhancements after acceptance, such as the addition of a cover page and metadata, and formatting for readability, but it is not yet the definitive version of record. This version will undergo additional copyediting, typesetting and review before it is published in its final form, but we are providing this version to give early visibility of the article. Please note that, during the production process, errors may be discovered which could affect the content, and all legal disclaimers that apply to the journal pertain.

Global geologic map of asteroid (101955) Bennu indicates heterogeneous resurfacing in the past 500,000 years

E. R. Jawin^{1,2*}, T. J. McCoy¹, K. J. Walsh³, H. C. Connolly Jr.^{4,5}, R.-L. Ballouz^{4,6}, A. J. Ryan⁴, H. H. Kaplan^{3,7}, M. Pajola⁸, V. E. Hamilton³, O. S. Barnouin⁶, J. P. Emery⁹, B. Rozitis¹⁰, D. N. DellaGiustina⁴, M. G. Daly¹¹, C. A. Bennett⁴, D. R. Golish⁴, M. E. Perry⁶, R. T. Daly⁶, E. B. Bierhaus¹², M. C. Nolan⁴, H. L. Enos⁴, and D. S. Lauretta⁴

¹ Smithsonian National Museum of Natural History, Washington, DC, USA

² Smithsonian National Air and Space Museum, Washington, DC, USA

³ Southwest Research Institute, Boulder, CO, USA

⁴ Lunar and Planetary Laboratory, University of Arizona, Tucson, AZ, USA

⁵ Department of Geology, School of Earth and Environment, Rowan University, Glassboro, NJ, USA

⁶ Johns Hopkins University Applied Physics Laboratory, Columbia, MD, USA

⁷ NASA Goddard Space Flight Center, Greenbelt, MD, USA

⁸ INAF-Astronomical Observatory of Padova, Padova, Italy

⁹ Northern Arizona University, Flagstaff, AZ, USA

¹⁰ The Open University, Milton Keynes, UK

¹¹ Centre for Research in Earth and Space Science, York University, Toronto, Canada

¹² Lockheed Martin Space, Littleton, CO, USA

*Corresponding author: Erica Jawin (jawine@si.edu)

Keywords: Bennu; rubble-pile asteroid; geologic map; OSIRIS-REx; surface evolution

Abstract

Global geologic maps are useful tools for efficient interpretation of a planetary body, and they provide global context for the diversity and evolution of the surface. We used data acquired by the OSIRIS-REx spacecraft to create the first global geologic map of the near-Earth asteroid (101955) Benu. As this is the first geologic map of a small, non-spherical, rubble-pile asteroid, we discuss the distinctive mapping challenges and best practices that may be useful for future exploration of similar asteroids, such as those to be visited with the Hera and Janus missions. By mapping on two centimeter-scale global image mosaics (2D projected space) and a centimeter-scale global shape model (3D space), we generated three input maps respectively describing Benu's shape features, geologic features, and surface texture. Based on these input maps, we defined two geologic units: the Smooth Unit and the Rugged Unit. The units are differentiated primarily on the basis of surface texture, concentrations of boulders, and the distributions of lineaments, mass movement features, and craters. They are bounded by several scarps. The Rugged Unit contains abundant boulders and signs of recent mass movement. It also has fewer small (<20 m), putatively fresh craters than the Smooth Unit, suggesting that such craters have been erased in the former. Based on these geologic indicators, we infer that the Rugged Unit has the younger surface of the two. Differential crater size-frequency distributions and the distribution of the freshest craters suggest that both unit surfaces formed ~10–65 million years ago, when Benu was located in the Main Asteroid Belt, and the Smooth Unit has not been significantly resurfaced in the past 2 million years. Meanwhile, the Rugged Unit has experienced resurfacing within the past ~500,000 years during Benu's lifetime as a near-Earth asteroid. The geologic units are consistent with global diversity in slope, surface roughness, normal albedo, and thermal emission spectral characteristics. The site on Benu where the OSIRIS-REx mission collected a regolith sample is located in the Smooth Unit, in a small crater nested within a larger one. So although the Smooth Unit is an older surface than the Rugged Unit, the impact-crater setting indicates that the material sampled was recently exposed. Several similarities are apparent between Benu and asteroid (162173) Ryugu from a global geologic perspective, including two geologic units distinguishable by variations in the number density of boulders, as well as in other datasets such as brightness.

1. Introduction

Asteroid (101955) Benu is a ~500-m-diameter primitive near-Earth asteroid (NEA) and the target of NASA's Origins, Spectral Interpretation, Resource Identification, and Security—Regolith Explorer (OSIRIS-REx) mission (Lauretta and DellaGiustina, et al., 2019; Lauretta et al., 2021). Spacecraft investigations of Benu have confirmed that it is a rubble pile (Barnouin et al., 2019)—a body that formed from the reaccumulated fragments of a larger, catastrophically disrupted parent body (e.g., Richardson, 2002; Michel and Ballouz et al. 2020)—with ubiquitous hydrated minerals on its surface (Hamilton et al., 2019; Simon et al. 2020). The surface of the asteroid is dominated by abundant boulders that vary in size, color, and spectral and thermal

properties (Walsh et al., 2019; DellaGiustina et al., 2020; Kaplan et al., 2020; Rozitis et al., 2020). The reshaping of Bennu's surface in the recent past has been dominated by small-scale creep (Jawin et al., 2020a; Barnouin et al., 2022), impact processing (Walsh et al., 2019; Bierhaus et al., 2022), and the evolution of individual boulders, including by thermal fracturing (Molaro et al., 2020; Delbo et al., 2022) and meteoroid impacts (Ballouz et al., 2020). The asteroid surface is also actively shedding mass, as documented by repeated particle ejection (PE) events of various magnitude (Lauretta and Hergenrother, et al., 2019; Hergenrother et al., 2020).

Bennu migrated to near-Earth space from its initial location in the Main Asteroid Belt (e.g., Bottke et al., 2015) and therefore provides a view into the geologic processes operating at different times in different locations in the Solar System. We created a global geologic map of Bennu to better understand the degree of variability of the surface, as well as the relationships (both spatial and temporal) between distinct regions and features on the surface of a rubble-pile asteroid. This global analysis helps to disentangle recent (and therefore more apparent) surface modification that may characterize Bennu's lifetime as an NEA from older and potentially less apparent processes that may have dominated Bennu's period in the Main Belt. Moreover, this map provides regional geologic context for the sample of Bennu's regolith that the OSIRIS-REx mission collected on October 20, 2020, and will return to Earth on September 24, 2023 (Lauretta et al., 2021).

To date, no global geologic map has been created for a rubble-pile asteroid, although mapping efforts are in progress for (162179) Ryugu (Miyamoto et al., 2019). We found that defining geologic units on Bennu's unconsolidated, boulder-rich surface posed challenges not encountered in mapping larger, monolithic planetary bodies, so this work serves both as a characterization of the global geology of Bennu and a proof of concept for mapping efforts by future missions to other small asteroids (e.g., the Hera mission to the binary Didymos (Cheng et al., 2018; Michel et al., 2018) and the Janus mission to two binary asteroid systems (Scheeres et al., 2020)). Our map of Bennu characterizes the broad-scale diversity of its surface but does not distinguish compositional or other properties of individual boulders that likely pre-date the formation of Bennu (i.e., were inherited from the parent body).

2. Data

2.1 Mosaics

Global image mosaics provided the basis for our definition of geologic units. Our primary mapping basemap was the global mosaic of Bennu generated from images collected during the Detailed Survey phase of the mission (Bennett et al., 2021) at a pixel scale of ~5 cm (**Figure 1A**). The Detailed Survey mosaic has global coverage at a higher spatial resolution and was photometrically normalized to 30° phase angle to remove illumination-dependent effects. However, the photometric normalization subdues the appearance of subtle topographic features such as crater rims and lineaments, as well as surface texture variations; in addition, there is a subtle image seam in the equatorial region (~20°N and ~5°S) that complicates mapping in this area.

As such, we supplemented morphologic analyses using a second mosaic made from images taken during the Approach phase of the mission (DellaGiustina and Emery et al., 2019) at a pixel scale of ~ 40 cm (**Figure 1B**). This Approach mosaic best highlights subtle topographic and surface texture variations, although image coverage only extends to $\sim 70^\circ$ N/S latitude. Mapped features were cross-referenced between both mosaics to ensure robust observations.

2.2 Shape model

We also used a global shape model produced from OSIRIS-REx Laser Altimeter (OLA) data (Daly et al., 2017; Barnouin et al., 2020; Seabrook et al., 2019), called OLA v20 (M. G. Daly et al., 2020), within the Small Body Mapping Tool (SBMT) (Ernst et al., 2018; <http://sbmt.jhuapl.edu/>). We mapped on the “Medium” resolution version of this shape model ($\sim 200,000$ 3-m facets), which is derived from the original 20-cm resolution OLA v20 shape model (M. G. Daly et al., 2020) and provided good spatial resolution while minimizing the contribution of individual boulder faces. We also used accompanying global datasets derived from the OLA v20 shape model including facet radius, or the distance from the center of the facet to the shape model center of figure (**Figure 1C**), and slope (see Section 2.3.1 below).

2.3 Additional datasets

After defining geologic units, we investigated whether they corresponded spatially to trends in other OSIRIS-REx datasets, including globally resolved maps of slope, surface roughness, normal albedo, thermal emission spectral characteristics, and thermal inertia. Each of these datasets is briefly described below.

2.3.1 Slope

Slope data are generated at each facet with each shape model in SBMT. Slope maps are sensitive to the baseline used, with smaller facets (i.e., higher-resolution shape models) incorporating steep faces of individual boulders (Scheeres et al., 2019). We therefore investigated slopes using three shape model resolutions in SBMT—Very Low (~ 6 -m facets), Medium (~ 3 -m facets), and Very High (~ 1 -m facets)—to understand the interaction between regional slopes and the increasing contribution from individual boulders.

Bennu has steeper slopes in the mid-latitudes of both hemispheres, with relatively flat regions near the equator (and also at the poles, Scheeres et al., 2019, see their Figure 3; Seabrook et al., 2019; Scheeres et al., 2020). In the Medium-resolution shape model with 3-m facets, for example, the average global slopes are 15.4° , but mid-latitude average slopes are $\sim 18^\circ$ and equatorial slopes (between $\sim 20^\circ$ N/S latitude) are $\sim 12^\circ$. The transition from the steep mid-latitude regions to the flat equatorial region coincides with the intersection of the rotational Roche lobe with the surface; the rotational Roche lobe is a region where the surface geopotential reaches a minimum equilibrium value owing to fact that the gravitational attraction and centripetal acceleration are balanced, leading to shallower surface slopes near the equator

(Scheeres et al., 2019; 2020). We used this Roche lobe–surface intersection boundary to define Bennu’s equatorial bulge, described in **Section 3.1**.

2.3.2 OLA surface roughness proxy

We investigated the global distribution of surface roughness by using an OLA-based proxy (M. G. Daly et al., 2020) (**Figure 2**). The roughness proxy was calculated by finding the standard deviation of OLA ranging values (from the full OLA point cloud) within a 30-cm-by-30-cm moving window. The resulting roughness map is reported in terms of standard deviation (in meters), where larger standard deviations correspond to rougher regions (up to ~ 9 m) and lower standard deviations correspond to smoother regions (effectively 0 m, where there is little scatter within the 30-cm window).

2.3.3 Normal albedo

The high-resolution map of normal albedo on Bennu was generated from PolyCam images by Golish et al. (2021). They created this map using ~ 6.25 cm/pix, short-exposure (~ 1.5 ms) images of the surface including the equator and mid-latitudes (up to $\sim \pm 50^\circ$) taken at low phase angles ($\sim 8^\circ$). The data were processed using a charge smear and radiometric correction, and images were photogrammetrically controlled to a shape model with a 5-cm ground sample distance. The mosaic therefore describes spatial variations in surface albedo across Bennu that can be correlated to specific features that were mapped such as boulders and craters.

2.3.4 Thermal emission spectral characteristics

An analysis of spectral data collected by the OSIRIS-REx Thermal Emission Spectrometer (OTES; Christensen et al., 2018) found that the surface of Bennu can be described by two spectral types, Type 1 and Type 2, that vary slightly in spectral slopes (from 1500 to 1090 cm^{-1}), band shapes (~ 987 and 814 cm^{-1}), and band depths ($\sim 440 \text{ cm}^{-1}$) (Hamilton et al., 2021). This map was generated by analyzing thermal infrared spectra at 40 m spatial scales collected at 12:30 pm and 8:40 pm local solar time. Hamilton et al. (2021) credited the variation seen across the two spectral types to the presence of thin deposits ($\sim 15 \mu\text{m}$) of fine-grained dust particles ($\lesssim 65 - 100 \mu\text{m}$) on top of larger particles ($> 100 \mu\text{m}$) leading to the appearance of transparency features in the OTES Type 2 spectra.

2.3.5 Thermal inertia and thermal roughness

The final datasets we compared to our geologic units were derived from thermophysical analyses of Bennu. Rozitis et al. (2020) generated global thermal inertia and thermal roughness maps using thermal emission data from both onboard spectrometers. We specifically investigated the maps made using data from the OSIRIS-REx Visible Infrared Spectrometer (OVIRS; Reuter et al., 2018) as they have a higher spatial resolution, with 20-m spectrometer spot sizes. Thermal emission was measured in the spectral range of 3.5 to 4.0 μm at seven different local times of day: 3:20 a.m., 6:00 a.m., 10:00 a.m., 12:30 p.m., 3:00 p.m., 6:00 p.m., and 8:40 p.m. Rozitis et

al. (2020) analyzed these spectra with a thermophysical model to simultaneously derive spatially resolved thermal inertia and thermal roughness maps.

3. Mapping methodology

Bennu's overall topographic relief is minimal, on the scale of tens of meters (Barnouin et al., 2019) and, in general, the surface lacks distinct stratigraphic contacts that would normally be used to define geologic units (e.g., young lava flows superposing ancient cratered highlands on the Moon). Defining unit boundaries on Bennu therefore requires a different methodology than what has been used to map other planetary bodies. As such, our mapping methodology is slightly different than the standard USGS mapping protocols—although we attempted to adhere to the USGS best practices where feasible. After initial trial-and-error mapping, we found that the abundance of boulders and lack of clear stratigraphic contacts resulted in mapping many small, disjointed units that did not efficiently or effectively characterize the surface of the asteroid. Therefore, we placed several requirements on the definition of geologic units: First, we required that the smallest unit be larger than the largest boulder (Roc Saxum, ~100 m diameter). Second, the perimeter of each unit should be minimized (to prevent small, narrow excursions of a unit boundary—e.g., we favored a circle over a star-shaped boundary). Finally, we sought to find the fewest number of units that could effectively characterize the surface of the entire asteroid.

We chose three distinct components of Bennu's surface that we mapped, analyzed, and integrated to define geologic units: (1) shape features, (2) geologic features, and (3) surface texture. Each of these three components was mapped separately in 2D and 3D using both the Approach and Detailed Survey mosaics for validation purposes, to minimize the potential for projection effects or observational biases to affect our mapping. Any disagreements between these separate mapping approaches were assessed and rectified prior to interpretation. 2D mapping was performed on spatially projected data using ArcGIS, and 3D mapping was performed on the OLA v20 shape model using SBMT. As our analysis integrated mapping in both ArcGIS and SBMT, we did not define a specific mapping scale that could be standardized across both software programs. This is because SBMT does not provide a mapping scale, unlike ArcGIS. However, we are confident that our unit boundaries and mapped features are robust and accurate due to our extensive validation process. For detailed unit boundary mapping in ArcGIS, we used a scale of 1:400 which was used for mapping in both mosaics. For similar detailed mapping in SBMT, we approximated a similar mapping scale. As noted above, to ensure the consistency in detail of all mapped boundaries, we had several independent mappers systematically identify and compare unit boundaries on both the Approach and Detailed Survey global mosaics, in both SBMT and ArcGIS. This validation process identified any discrepancies between mappers and/or in the level of detail in unit boundaries, which were subsequently rectified.

In the maps presented here, we adhered to USGS Federal Geographic Data Committee (FGDC) Digital Cartographic Standards for Geologic Map Symbolization where feasible. Given Bennu's very small size and rubble-pile nature, certain geologic features do not have

standardized symbology (e.g., PE source regions, saxa). Therefore we use original symbology when standard options are not available.

4. Mapping

4.1 Shape feature mapping

Bennu contains three dominant large-scale features that contribute to the non-spherical shape of the body: (1) the equatorial bulge, (2) several longitudinal ridges, and (3) troughs between the longitudinal ridges.

The equatorial bulge is a distinct feature in Bennu's global spherical harmonics (Barnouin et al., 2019; M. G. Daly et al., 2020; Roberts et al., 2021) and is apparent in the global shape model (e.g., **Figure 1C**) and global slope maps (Scheeres et al., 2019). However, there is no distinct morphologic contact that defines the equatorial bulge. To define the bulge we therefore relied on the facet-radius data and the intersection of the rotational Roche lobe with the surface. Because surface slopes depend on the length scale, we did not define the equatorial bulge purely on the basis of slope values. Instead, we traced a contour line along the minimum facet radius value (using a map of radius contours) that encompassed the largest region inside the Roche lobe and minimized the region outside the Roche lobe (in the steeper-sloped mid-latitudes). For this boundary we used the facet radius contour at 250 m (solid line, **Figure 3**). The region enclosed by the 250-m facet radius value incorporates the flat-sloped equatorial region and covers ~37% of the total surface area of Bennu (total surface area: 0.787 km^2 , M. G. Daly et al., 2020). The equatorial bulge includes most of the surface of Bennu between 20°N/S , although the latitude of the boundary varies from as low as 6°S ($\sim 60^\circ\text{E}$) to as much as 26°N ($\sim 355^\circ\text{E}$). This variability is related to the irregular surface topography of the region, which includes several large crater rims.

The longitudinal ridges were initially identified based on analyses of the spherical harmonics of Bennu's shape (Barnouin et al., 2019). This initial characterization found a root-mean-square amplitude of $\sim 10 \text{ m}$ in the degree-4 sectoral shape in spherical harmonics, with a maximum relief of 25 m (from the crest of a ridge to the base of an adjacent troughs), and lengths ~ 400 to 780 m. Additional analyses by M. G. Daly et al. (2020) confirmed the presence of four longitudinal ridges in both hemispheres and the equatorial region (dashed lines, **Figure 3**) and found that portions of the ridges in the southern hemisphere have been obscured due to surface material transport, which has contributed to a higher degree-2 harmonic. Troughs were initially described by Barnouin et al. (2019) as depressed regions between the longitudinal ridges.

While approximate locations for the longitudinal ridges were given in Barnouin et al. (2019) and M. G. Daly et al. (2020) based on analyses of the spherical harmonics (dashed lines, **Figure 3**), detailed mapping of the extent and spatial distribution of the ridges had not been performed. We therefore used the approximate locations of the longitudinal ridges from M. G. Daly et al. (2020) as a starting point to map the ridges and troughs in detail. Similar to the equatorial bulge, the longitudinal ridges have minimal surface morphologic expression and are

apparent in the global DTM, but the longitudinal ridges appear less distinct in maps of facet radius compared to the equatorial bulge. Though muted, the longitudinal ridges are subtly apparent by their higher topography compared to the surrounding regions at similar latitudes.

We defined their locations using OLA-derived maps of facet radius based on 5-m radius contours. We then mapped regions of locally higher elevation ≥ 50 m wide and oriented N-S. To distinguish the features we mapped from the features previously identified from spherical harmonics, we refer to our mapped longitudinal ridges as *high-standing regions* and troughs as *low-lying regions*. Additionally, we mapped low-lying regions as all regions not covered by high-standing regions, which is consistent with the previous definition of the troughs as depressed regions between the longitudinal ridges (Barnouin et al., 2019). Therefore, we classified Bennu's entire surface as either a high-standing or low-lying region.

Our mapped high-standing regions are outlined in **Figure 4** (and **Supplementary Figure 1** mapped on the shape model in 3D). Our analysis agrees with previous descriptions of Bennu's shape being characterized by ridge and interridge (trough) regions, and we identified high-standing regions in the same approximate locations as the previously identified longitudinal ridges (Barnouin et al., 2019; M. G. Daly et al., 2020)— although the specific number and distribution of high-standing regions that we find are somewhat different than suggested in the previous analyses. For example, our results show that there is one high-standing region in the northern hemisphere that spans the north pole and extends south across the equator to $\sim 30^\circ\text{S}$ (at $\sim 100^\circ\text{E}$ and 300°E), and a second high-standing region in the southern hemisphere centered $\sim 20^\circ\text{E}$ that extends from the south pole up to $\sim 30^\circ\text{N}$. A third, smaller high-standing region is present at $\sim 200^\circ\text{E}$ that appears to be restricted mostly to the equatorial region, extending between $\sim 40^\circ\text{N}$ and S. Unlike the distribution of longitudinal ridges in M. G. Daly et al. (2020), we do not find any high-standing region that reaches both poles (this is not due to latitudinal bias, as the analysis relied on the facet radius data derived from the OLA shape model). High-standing regions cover approximately 46% of the surface of Bennu.

Low-lying regions were mapped as all other regions not covered by high-standing regions (**Supplementary Figure 2**). We did not separate the locations between high-standing regions into individual low-lying regions; rather we defined the entire non-high-standing region as a low-lying region. However, some portions of the low-lying regions are more depressed than others, probably indicating the presence of large, degraded impact craters (e.g., $\sim 60^\circ\text{E}$, 60°N). Low-lying regions are oriented N-S between the high-standing regions, consistent with the description of troughs by Barnouin et al. (2019), and include large swaths of the mid-latitude regions in both hemispheres (~ 30 - 60°N and S) as well as the equator, leading to a slightly larger surface area than that of the high-standing regions: $\sim 54\%$ of Bennu's surface.

The mapped high-standing and low-lying regions do not appear to be strongly affected by the presence or boundary of the equatorial bulge. Both span the mid-latitudes and equatorial region, although high-standing regions on the equatorial bulge are wider than in the mid-latitudes (conversely, low-lying regions are narrower on the equatorial bulge and wider in the mid-

latitudes). No other correlations were noted between the distribution of high-standing regions, low-lying regions, and the equatorial bulge.

4.2 Geologic feature mapping

We mapped several major geologic features on the surface: craters, lineaments, boulders (labeled as *saxa*, singular *saxum*), features interpreted to have formed from mass movement, and PE source regions. We discuss each of these below. We also include the location of the OSIRIS-REx sample site, Nightingale, to provide global geologic context for the returned sample.

4.2.1 Craters

Craters were previously identified and mapped (Bierhaus et al., 2022) using images acquired by the OSIRIS-REx Camera Suite (OCAMS; Rizk et al., 2013; Golish et al., 2020) and digital terrain models constructed from OLA data. This analysis resulted in a database of 1560 craters ranging from <1 m to over 200 m in diameter (Bierhaus et al., 2022). Most craters on Bennu lack the sharp raised rims and associated ejecta deposits (Bierhaus et al., 2022) that are typical of craters on larger planetary bodies. Many of the small craters (less than ~20 m) were identified based on a lack of boulders in their interiors (containing instead concentrations of fine-grained regolith) (Walsh et al., 2019), although this is not true of all small craters (for example, craters in boulders; Ballouz et al., 2020).

Craters in this database were analyzed to determine whether they exhibited a clear topographic expression, i.e., a depressed interior and/or a raised rim around part or all of the crater (R. T. Daly et al., 2020). This process removed several candidate craters (e.g., circular features with no topographic signature) from the initial global catalogue. For the global geologic map, we included craters 10 m in diameter and larger that contained a clear topographic signature, which includes 153 mapped craters ranging in size from ~10 m to ~160 m in diameter (R. T. Daly et al., 2020) (**Figure 5, data available in Jawin et al., 2022a**). Small craters (<10 m) were not included on the global map to maximize readability, but are important for studying the crater retention age of the surface (Bierhaus et al., 2022) and will be discussed in detail in **Section 7**.

The geologic feature map contains 75 craters between 10 and 20 m, and 78 craters > 20 m. The largest crater in this catalogue, Minokawa Crater, is ~160 m in diameter and located near the equator (centered near 270°E) (see **Supplementary Figure 3** for a map of all named features on Bennu). Craters are globally distributed, although initial mapping of craters on Bennu (Walsh et al., 2019) noted an apparent concentration of large craters in the equatorial region relative to the mid-latitudes. We find that of the largest craters on Bennu (>60 m diameter, 20 craters), 50% (10 craters) are located on the equatorial bulge (compared to 35%, 7 craters, in the northern hemisphere and 15%, 3 craters, in the southern hemisphere outside the equatorial bulge). As discussed above, several large impact craters correspond to regions we mapped as low-lying regions, including craters centered near 60°E, 60°N; near 180°E, 60°N; and near 160°E, 30°N. The association of craters with other mapped geologic features will be discussed in the following

sections, and the spatial distribution of craters and possible surface ages will be examined in **Section 7**).

4.2.3 Lineaments

Lineaments were first identified in an early, incomplete database developed by Perry et al. (2019) based on analysis of OCAMS images from the Approach and Detailed Survey phases of the mission. Lineaments include features such as ridges, scarps, or other morphologic expressions with linear alignments. To be classified as a candidate lineament, features were required to be visible in at least two OCAMS images taken at different phase angles to ensure that they were not the result of illumination or projection effects. Each candidate lineament was then validated by using an early, lower-accuracy image-derived global shape model in SBMT to confirm the presence of a clear topographic expression.

To update these analyses, we filtered the database of lineaments mapped by Perry et al. (2019) and removed any features not obvious in the image mosaics. We also required that the lineament be discernable in the shape model and have a quantifiable elevation change on both its sides, not just the lineament itself (which would be generated, for example, from a chain of boulders). We did not include any linear features that correspond to large crater rims, as craters were mapped as separate geologic features. We also required lineaments to have a minimum length of 100 m, the approximate diameter of the largest boulder on Bennu (Roc Saxum), to prevent the detection of any linear features originating from individual boulder edges. The high-standing regions and low-lying regions were not mapped as lineaments as they have minimal surface morphologic expression, are much broader in spatial scale, and they were previously mapped in the analysis of Bennu's shape features.

In addition, several candidate lineaments that appeared to be contiguous linear features were later resolved in higher-resolution images to be several individual boulders in an apparently linear pattern. We did not include these features in our database, and instead included only structural lineaments (e.g., scarps). This does not preclude the presence of other structural elements (similar ridges of boulders occur on Itokawa and Eros (Cheng et al., 2007) and are interpreted as evidence of structure), but other structural lineaments are not immediately obvious without detailed assessment of high-resolution digital terrain models.

We identified five lineaments on Bennu (**Figure 5**, **Table 1**) that are ~100 to 200 m in length. Lineaments are oriented mostly N-S, except one that is oriented E-W, and all are curvilinear in extent. We are confident that the prevalence of N-S trending lineaments is not due to observational bias, as we validated all lineaments using the OLA shape model. The mapped lineaments all resemble scarps, with one side of the lineament at a slightly lower facet radius value than the other, and accumulations of boulders present on the low-facet radius sides. The boulder-rich sides of the lineaments are all at lower facet-radius values than the smoother, higher-facet-radius sides, with relief of ~5 m (up to 10 m). The most distinct scarp on Bennu (lineament 3, **Table 1**) is also the longest lineament (195 m, **Figure 6**) located at ~230°E. The higher-facet-radius side of this scarp (west of the lineament) is ~10 m higher than the area

immediately to the east, which contains the highest boulder concentration on Bennu (Walsh et al., 2019, their Fig. 2; named Tlanuwa Regio). The extremely rough and boulder-rich surface immediately adjacent to the scarp in Tlanuwa Regio suggests that lineament 3, as well as the other mapped scarps, formed via slope collapse.

Adjacent lineaments may have formed and/or evolved in concert; for example, lineaments 3 and 4 are nearly contiguous (**Figure 5**), and may have originated as parts of a single larger scarp that spans nearly all of Bennu's circumference. Conversely, they may have formed as smaller distinct scarps, and over time have evolved towards one another. Lineaments 1 and 2 have the same N-S orientation and span similar latitudes. Their down-slope sides are reversed (E of lineament 1, W of lineament 2), such that they form a local depression centered $\sim 140^\circ\text{E}$ that contains abundant boulders; this depression approximately corresponds to a mapped region of the high-standing regions (**Figure 4, Supplementary Figure 2**). It is unclear whether these two scarps formed concurrently, but their evolution has created a distinct morphologic region on Bennu's surface.

4.2.2 Saxa

As Bennu is a rubble-pile asteroid, boulders are by far the most common geologic feature on the surface, with thousands of boulders >20 cm in longest dimension (DellaGiustina and Emery et al., 2019). Several previous analyses have mapped the distribution and properties of rock particles on Bennu at different scales (e.g., DellaGiustina and Emery et al., 2019; Walsh et al., 2019; DellaGiustina et al., 2020; Jawin et al., 2020a; Burke et al., 2021). Including the location of every mapped boulder on Bennu is impractical for a global geologic map, so we only mapped boulders ≥ 20 m in diameter (longest dimension). We relied on previous mapping by Jawin et al. (2020a) of the largest boulders on Bennu (≥ 30 m), which was done by examination of the Approach and Detailed Survey global mosaics and validated using the OLA shape model. Partly buried boulders were mapped by Jawin et al. (2020a) if the visible portion of the boulder exceeded 30 m in diameter. This 30-m-diameter threshold was used because boulders larger than this size were readily apparent at all latitudes of Bennu in the image mosaics and the shape model available at the time. We incorporated these previously mapped boulders into our database and used the same methodology to identify additional boulders between 20 and 30 m in diameter, such that all boulders ≥ 20 m in diameter were mapped.

Several analyses have studied the distribution and state of burial of large boulders on Bennu. DellaGiustina and Emery et al. (2019) first noted an underabundance of the very large boulders in the equatorial region, implicating an excavation and/or burial process occurring on Bennu. Jawin et al. (2020a) further investigated this trend and found that of the very large boulders (≥ 30 m diameter), only 18% (three) are located in the equatorial region. In addition, boulders in the mid-latitudes appear to be perched on the surface or partly buried on their upslope faces (**Figure 7B**), while their downslope faces can have up to several meters of relief from the surrounding terrain (Jawin et al., 2020a). The most extreme example of a perched boulder (Benben Saxum) reaches several tens of meters higher than the surrounding surface

(Barnouin et al., 2019) and is the only boulder visible from Earth-based radar analyses (Nolan et al., 2013). In comparison, very large equatorial boulders appear flush with the surface, with <1 m of relief and morphologies consistent with burial from multiple directions (Jawin et al., 2020a). The variable distribution and degree of burial of boulders with latitude was attributed by Jawin et al. (2020a) to equatorially migrating material—they argued that the transport of ~ 10 m of material from the mid-latitudes, and its deposition near the equator in an equivalent layer ~ 5 m thick, could have exposed and concentrated large boulders in the mid-latitudes and buried equatorial boulders, resulting in the observed distribution.

The map of saxa in this work shows that large boulders are widely distributed on Bennu, with 36 boulders ≥ 20 m in diameter that range in size up to ~ 100 m (**Figure 7A; data available in Jawin et al., 2022b**). Unlike the analysis of only boulders >30 m by Jawin et al. (2020a), we find there are approximately the same number of boulders ≥ 20 m per unit area on the equatorial bulge as in the higher-latitude regions. The map of saxa shows a hemispheric dichotomy in boulder concentration though: 64% (23 boulders) of the mapped boulders ≥ 20 m diameter are present in the southern hemisphere, and 36% (13 boulders) in the northern. This hemispheric difference may be due to different patterns of mass movement between the two hemispheres, and/or could be due to a primordial asymmetry of boulders (M. G. Daly et al., 2020; Jawin et al., 2020a).

4.2.4 Mass movement morphologies

Morphologies consistent with mass movement of regolith and rocks on Bennu's surface were previously mapped (Jawin et al., 2020a), and we included these in our map of geologic features. These features were identified by examining OCAMS images and the Approach and Detailed Survey mosaics, and they were mapped on a global shape model in SBMT. The apparent direction of motion associated with each mass movement feature was determined based on the relative stratigraphy at each location, where stratigraphically higher material was interpreted to be younger (e.g., if a boulder is partly covered by regolith, it was assumed that the regolith is stratigraphically younger). Jawin et al. (2020a) only mapped a mass movement feature if the direction of apparent motion of the feature could be determined, as these data were investigated for the relationship of motion relative to local slopes. Owing to the small spatial scale of virtually all the identified mass movement features, each feature is marked only as an arrow, rather than an outline around the extent of each feature. One exception, a smooth lobate deposit (centered $\sim 270^\circ\text{E}$, 10°S), is large in spatial extent (over 90 m wide, compared to the small mass movement features on the scale of ~ 1 m) and has distinct boundaries; therefore, this feature was outlined as a polygon in our map, rather than indicated with a single arrow.

We included the 87 mass movement features identified in Jawin et al. (2020a) (**Figure 7A, data available in Jawin et al., 2020b**). Identified morphologies include partly buried boulders (e.g., **Figure 7B**), rock fragments of various sizes perched on other boulders, long-axis particle alignment, rock imbrication, particle size grading, and one large-scale smooth lobate deposit (approximately 90 m wide) located inside Minokawa Crater on Bennu ($\sim 270^\circ\text{E}$, 10°S ,

Figure 7C). The smooth lobate deposit has been previously characterized as the only well-preserved landslide or mass flow feature on Bennu (Walsh et al., 2019; Jawin et al., 2020a). Walsh et al. (2019) suggested the mass flow feature originated from outside (west of) the host crater and moved eastward, overtopping the rim of Minokawa Crater and terminating in the crater interior, depositing ~6 m of material. The large N-S scarp to the west of the smooth lobate deposit (lineament 3, **Figure 5**) may represent the landslide headwall from which it originated (Jawin et al. 2020a).

The features identified by Jawin et al. (2020a) formed due to mass movement at various spatial scales, from creep of individual particles to the single large mass flow. Several large craters contain morphologic evidence of smaller-scale mass movement in their interiors, including slumps and accumulations of boulders. Additional evidence of small-scale creep is evident on the surface in the form of terraces (Barnouin et al., 2022). Mass movement features are globally distributed, and the interpreted direction of motion is generally N-S, oriented towards the equator, which may have led to the excavation and concentration of large boulders as discussed in the preceding section. All visible instances of mass movement (yellow arrows, **Figure 7A**) are in the current downslope direction, suggesting that they formed recently—during the present spin period epoch, which sets the global slopes—specifically within the past ~200,000 years (Jawin et al., 2020a).

4.2.5 Particle ejection source regions

Several of the PE events observed by the OSIRIS-REx spacecraft (Lauretta and Hergenrother, et al., 2019; Hergenrother et al., 2020) were sufficiently large and opportunely timed to be imaged multiple times by the navigation camera, enabling determinations of individual particle trajectories, velocities, and ejection times, as well as determination of the expected radiant points on the surface of Bennu to within a few degrees (Leonard et al., 2020; Pelgrift et al., 2020; Hergenrother et al., 2020; Chesley et al., 2020). We included the locations of source regions for the five largest observed PE events (those with at least 20 observed ejected particles, with a maximum of ~200 particles) in our mapped geologic features.

Analysis of OCAVIS images taken of the PE source regions before and after the events showed no resolvable surface change that could be credited to the PE events (Lauretta and Hergenrother et al., 2019). This is not surprising given that energies associated with even the largest PE events were low (on the order of millijoules), with velocities of a few centimeters to a few meters per second (Hergenrother et al., 2020). However, despite the lack of resolvable surface change induced by the PE events, we still include the PE source regions on the geologic feature map, as they indicate regions of documented present-day surface activity on Bennu.

The radiant points for the five largest PE events are shown in **Figure 7A** and **Table 2**. As the 6 January event did not have sufficient data to identify a unique source region solution, both the “near” and “far” solutions were included (white dashed line, **Figure 7A**). PE source regions occur at two similar latitude regions: the northern hemisphere around 20°N (three events), and the high latitudes of the southern hemisphere (~65°S, two events). The estimated ejection times

for these events mostly occurred in the late afternoon or early evening, with four events occurring between 15:22 and 18:06 local solar time (the exception is the 13 September event occurring at 10:13) (see Table 2 in Hergenrother et al., 2020). The five mapped events are widely distributed with longitude. The three northern hemisphere source regions are located within the low-lying regions, and the three southern hemisphere events (including the two radiant points for the 6 January event) are on the high-standing regions. No spatial associations were found with other mapped geologic features. Smaller events (2 – 8 particles) were frequently observed with ejection locations mostly in the mid-latitudes ($\sim 30\text{--}40^\circ$, Hergenrother et al., 2020), which we did not include on the map.

4.2.6 Distribution of geologic features on Bennu

The distribution of geologic features on Bennu's surface (**Figure 8**) provides insights into the characteristics of the surface that were necessary for defining geologic units. Lineaments demarcate broad, boulder-rich regions which likely formed via slope collapse. Adjacent or associated lineaments (e.g., lineaments 1 and 2; lineaments 3–5) indicate regions with distinct boundaries that contain clear concentrations of boulders distinct from the surrounding smoother surface. Saxa are most abundant in the mid-latitudes, and may have become exhumed over time—these large boulders are also spatially correlated with small-scale mass movement features recording the motion of material towards the equator. Large craters contain collections of boulders that may have accumulated over time and show evidence for small-scale mass wasting (wall slumps) and large-scale resurfacing and infilling (the smooth lobate deposit). Taken together, these geologic features show that Bennu's surface has been evolving over time, which has affected the distribution of boulders and craters on its surface. The geologic feature map (**Figure 8**) is therefore instrumental in defining geologic units on Bennu's surface, and in determining the relative ages and formation mechanisms for each unit.

4.3 Surface texture mapping

Regions with distinct morphologic expressions of surface texture were identified by visual inspections of the Approach and Detailed Survey global mosaics. Our surface texture mapping followed similar guidelines as the regional physiographic classification of El-Maarry et al. (2015, 2016) for comet 67P/Churyumov-Gerasimenko (67P), where distinctive, coherent regions were outlined based on “clear and major morphological and/or topographical boundaries”. One difference in performing such a regional physiographic classification is that Bennu lacks many distinct morphological and topographical boundaries. Therefore, for the surface texture mapping we first identified only the most morphologically distinct regions, and regions where boundaries were clearly apparent. We then examined the remaining unmapped regions to determine whether they belonged to a distinct physiographic group, or were more likely a mixture of the more distinct mapped groups (and/or lacked distinct boundaries).

We identified the most morphologically distinct regions of Bennu's surface, which fall into two categories: (1) regions with smooth or knobby surface textures, which contain relatively

few boulders, and (2) regions with rugged surfaces that contain abundant boulders (**Figure 9A**). The dominant discriminator between these two physiographic regions is the apparent abundance (or absence) of boulders, leading to rugged (or smooth to knobby) surfaces (**Figure 9B-C**). Both regions are widely distributed across the equatorial and mid-latitude regions. As we primarily used the Approach mosaic for the surface texture mapping, we did not include the polar regions, but truncated the mapped regions at $\sim 70^\circ\text{N/S}$.

The rugged regions have a general N-S orientation and are mostly present in the mid-latitudes, although several regions extend to the equator. The smooth/knobby regions have no preferred orientation, with approximately half having a N-S orientation and the others having an E-W orientation. Smooth/knobby regions are located in both the mid-latitudes and equatorial region. We mapped more rugged regions than smooth/knobby regions on Bennu, which is unsurprising given Bennu's rubble-pile nature and the abundance of boulders on the surface. Additionally, rugged, boulder-rich regions are more distinct and often have clear boundaries with surrounding smoother regions, making them easier to identify (for example, Tlanuwa Regio)—which may also contribute to the higher number of mapped rugged surface texture regions.

The remaining portion of Bennu's surface did not fall into the distinctly rugged or smooth/knobby physiographic group, and/or did not have distinct boundaries that were easily mapped. Upon examination we determined that these regions belonged to an intermediate physiographic group, with surface textures ranging from smooth/knobby to rugged, and with variable boulder concentrations. We therefore marked these regions as “intermediate” surface texture regions that were not sufficiently distinct to belong to either the smooth/knobby or the rugged regions (corresponding to the unmapped regions in **Figure 9A**).

5. Geologic units

We assumed similar principles of unit definition as those of Giacomini et al. (2016) for comet 67P, where regions with similar morphology, surface texture, stratigraphic position, and possible common origin are mapped as the same unit. Therefore, while surface texture (as discussed in the previous section) is a major input in determining the geologic units, geologic units may have slightly different boundaries than the physiographic regions identified in the surface texture mapping, although the two maps are complementary (e.g., Giacomini et al., 2016; Lee et al., 2016). To define the geologic units on Bennu, we identified regional variations in the maps of shape features, geologic features, and surface texture and outlined broad-scale regions with co-occurring characteristics (e.g., similar surface texture and concentration of geologic features). We then refined unit boundaries using the high-resolution Detailed Survey mosaic to identify specific, potentially subtle, contacts or surface texture variations. As with generating the three input maps, for validation we repeated the unit definition on projected mosaics in ArcMap and on mosaics draped over the shape model in SBMT, which ruled out projection effects or potential observational biases. Conflicting unit boundaries were assessed using both global mosaics in 2D and 3D, as well as topographic data from the shape model.

We integrated the three maps of surface texture, geologic features, and shape features to characterize Bennu's surface into geologic units, following the process described in Section 3.4 (**Supplementary Figure 4**). We identified two geologic units that together cover the entirety of Bennu's surface, which we name the Smooth Unit and the Rugged Unit (**Figure 10**). We deliberately follow similar terminology as for the two end-member surface texture physiographic groups described above because surface texture captures most of the variation between the two units.

The two units can be distinguished most readily by regional variations in the concentrations of boulders, both at very large sizes (i.e., mapped saxa ≥ 20 m) as well as at the meter and sub-meter scale, and these regions are bound in several locations by lineaments. The Smooth Unit covers both poles of Bennu to $\sim 70^\circ\text{N/S}$, with elongated regions extending towards the equator, and one region (centered $\sim 70^\circ\text{E}$) extending into the mid-latitudes of the opposite hemisphere. The Smooth Unit does not extend continuously from pole to pole anywhere. The Smooth Unit covers $\sim 44\%$ of Bennu's surface.

The Rugged Unit occurs in elongated N-S-oriented regions, although it spans only the equatorial region into the mid-latitudes, terminating at $\sim 70^\circ\text{N/S}$. Note that this termination at $\sim 70^\circ\text{N/S}$ also corresponds to the boundary of our surface texture mapping. However, we are confident that this latitude corresponds to a real unit boundary (rather than an effect of mapping bias), as we confirmed the presence of this boundary in the Detailed Survey mosaic, which has full polar coverage. We are therefore confident that the Rugged Unit does not extend past $\sim 70^\circ\text{N/S}$. The Rugged Unit covers more of the equator than the Smooth Unit does, and therefore it has a larger surface area, covering 56% of Bennu's surface. Comparing these to the input maps of surface texture, geologic features, and shape features highlights the distinction in the two units and helps to characterize the surface diversity on Bennu, and will be briefly discussed.

5.1 Comparing geologic units to the surface texture map

Surfaces in the Smooth Unit are, as the name suggests, morphologically smooth and lacking in large collections of boulders, following similar physiographic properties as the smooth/knobby surface texture map. Because of this, the Smooth Unit includes all the mapped smooth/knobby surface texture regions (**Figure 11**) except for one, centered at $\sim 270^\circ\text{E}$, 5°S , as discussed below. Additional portions of Bennu's surface are included in the Smooth Unit which belong to the intermediate surface texture group. These intermediate physiographic regions may be slightly rougher and/or contain more boulders than the yellow outlined regions in **Figure 11**, but they were not sufficiently rough or boulder-rich to be included in the Rugged Unit. In addition, these regions did not contain any clear boundaries with other portions of the Smooth Unit.

The one region of smooth/knobby surface texture not included in the Smooth Unit ($\sim 270^\circ\text{E}$, 5°S) corresponds to the smooth lobate deposit located in Minokawa Crater (**Figure 8**). This lobate deposit is texturally smooth and distinct, with clear boundaries. However, it is < 100 m in diameter, the minimum diameter we required for a geologic unit, and the deposit is located

in a distinctly rugged region which could not be mapped as a contiguous portion of the larger adjacent Smooth Unit. As such, we did not map this feature into the Smooth Unit.

The Rugged Unit has rougher surface textures and contains all the mapped rugged surface textural regions (red regions in **Figure 11**), which include the most distinct boulder-rich regions on Bennu. As with the Smooth Unit, the Rugged Unit incorporates regions of the intermediate surface texture group. In several locations, the Rugged Unit connects several textural regions that were mapped as disparate accumulations of boulders (e.g., the region near 330°E, 60°N; near 170°E, 30°N) which, after assessing the other input maps, we determined belonged to the same unit.

We examined the intermediate surface texture regions to determine if adding a third geologic unit was necessary. However, we determined that these texturally-intermediate regions do not have sufficiently distinct properties, either in surface texture, geologic feature distribution, or shape feature characteristics, nor do they have clear enough boundaries or stratigraphic contacts, to merit classification as a distinct third geologic unit. Therefore, after distinguishing the two units and comparing them to our mapped surface textural regions, we are confident that the two units robustly describe the dominant variation on the asteroid's surface.

5.2 Comparing geologic units to the geologic feature map

The distribution of mapped geologic features was critical to distinguishing the two geologic units and understanding their evolution and relative ages (**Figure 12**). Geologic features and geologic units are shown on the 3D shape model in **Supplementary Figure 5**.

Every mapped lineament corresponds to a geologic unit boundary. These unit-defining lineaments trace contacts between relatively smooth regions and regions with high concentrations of boulders. Most lineaments are also located on or near boundaries of the high-standing regions and low-lying regions (however, surface texture does not have a strong correlation with high-standing regions, low-lying regions, or the equatorial bulge.)

Saxa are almost entirely located within the Rugged Unit (89%, 32 boulders, **Table 3**), which is expected as the Rugged Unit was defined partly based on the presence of saxa (and concentrations of smaller boulders below the mapping threshold of 20 m). The mass movement features identified by Jawin et al. (2020a) are also concentrated in the Rugged Unit (85%, 74 features, **Table 3**). These associations strongly suggest that the Rugged Unit has experienced resurfacing due to mass movement, while the relative paucity of mass movement in the Smooth Unit may suggest that mass movement was less common and/or smaller in scale in that unit.

The Smooth Unit contains 60% of all mapped craters (90 craters) compared to only 40% (61 craters) in the Rugged Unit; the Smooth Unit also contains more small (10–20 m) craters (**Table 3**). When scaled for surface area, there is still a factor of ~2 more craters per unit area in the Smooth Unit than the Rugged Unit. There is a latitudinal effect present in the crater distribution, where more large craters are located on the equatorial bulge compared to the mid-latitude and polar regions. However, this latitudinal effect does not explain the crater distribution between the two units, as the Rugged Unit spans more of the equatorial region, and includes

most of the equatorial craters (**Figure 12**), while the Smooth Unit includes most of the polar regions. The difference in crater distribution may indicate differences in resurfacing histories of the two units, as well as potential differences in responses to impacts, specifically the process of impact armoring. This will be discussed further in **Section 7**.

The PE source regions for one event and the near radiant point from the 6 January event are located in the Smooth Unit, while the source region for the other three events and the far radiant point from the 6 January event are located in the Rugged Unit.

5.3 Comparing geologic units to the shape feature map

The map of shape features does not correlate significantly with the two other input maps of surface texture and geologic features, and so the shape feature map (including the high-standing regions, low-lying regions, and equatorial bulge) did not play a significant role in defining geologic units. The high-standing regions, low-lying regions, and equatorial bulge are all intersected by both smooth and Rugged Units (**Figure 13**). The Smooth Unit is present on slightly more than half of the equatorial bulge and the high-standing regions, and slightly less than half of the low-lying regions (**Table 4**).

One similarity that does exist between the high-standing regions and low-lying regions and the geologic units is the general N-S orientation. This similarity does not extend to the map of surface texture, in which the smooth/knobby regions did not all have a N-S orientation. In addition, equivalent boundaries between high-standing regions and the geologic units are present in a few locations (e.g., 160°E, 30°S; 220°E, 20°S; 310°E, 30°S), most of which also correspond to the location of mapped lineaments.

The equatorial bulge in particular does not appear to have been a major control on Benu's surface evolution as mapped in this work. It has not affected the presence or distribution of high-standing and low-lying regions, as discussed in **Section 4.1**, and there is little spatial correlation with the geologic unit boundaries. A few locations in the geologic units do terminate near the boundary of the equatorial bulge (e.g., 10°E, 20°S; 160°E, 20°N; 240°E, 10°N); however, most of the geologic unit boundaries cross over the equatorial bulge and show little variation on versus off the bulge.

6. Comparison with other global datasets

Here we highlight similarities and differences between our global geologic map and other spatially resolved global datasets based on OSIRIS-REx spacecraft observations, including slope, surface roughness, normal albedo, thermal emission spectral characteristics, and thermal inertia.

6.1 Slopes

As previously noted, the global slopes on Benu follow a latitudinal trend, with steeper mid-latitudes and a flatter equator (Scheeres et al., 2019). Because the two geologic units span the poles, mid-latitudes, and equatorial regions, deriving an average slope value for each unit conflates their contributions. However, despite this global trend, slopes are on average steeper in

the Rugged Unit than the Smooth Unit—although the magnitude of the difference changes with the slope baseline (**Table 5, Supplementary Figure 6**). Average slopes measured on the Very Low resolution SBMT shape model, with ~6-m facets, show almost identical median values in both geologic units (1° difference)—this low-resolution shape model reflects the broad-scale latitudinal trends of the asteroid. Conversely, the Very High resolution shape model with ~1 m facets shows a larger difference (8°) in average slope. The shorter baseline of the Very High resolution shape model highlights individual steep boulder faces that are more abundant in the Rugged Unit.

The standard deviations (1σ) of slopes in the two units are large relative to the median values, which reflects the latitudinal variation in slope values. However, histograms of the slope distributions (**Supplementary Figure 6**) show right-skewed distributions in both units, with larger tails in the Rugged Unit at all three shape model resolutions. The difference in histogram distribution shape is most evident in the Very High resolution shape model (**Supplementary Figure 6C**), further illustrating the increased role of individual steep boulder edges in the Rugged Unit, highlighted at the smallest spatial scale.

6.2 Surface roughness

Because the major discriminator between the two geologic units is surface texture and boulder abundance—which are intimately related to surface roughness—we sought to quantify the roughness properties of the two units using the OLA surface roughness proxy map (**Figure 14A**). Rougher regions are clearly distinguished from smoother regions in the global roughness proxy map by the geologic unit boundaries, with apparently rougher regions corresponding to the Rugged Unit, and less rough regions, including the polar regions, corresponding to the Smooth Unit. However, the median roughness of the Smooth and Rugged Units are the same within uncertainty (Smooth Unit: 0.25 m; Rugged Unit: 0.36 m), due to large standard deviations (Smooth Unit: 0.33 m; Rugged Unit: 0.68 m)—highlighting the heterogeneity of Bennu’s surface. Despite the similar median roughness in both units, histograms of surface roughness both show right-skewed distributions, with a larger tail in the Rugged Unit, similar to the distributions of surface slopes. The similar shapes of the distributions in surface roughness and slope data is unsurprising given the close spatial scale between surface roughness (~30 cm) and short-baseline (~1 m) slope, and the fact that both datasets are controlled largely by individual boulder faces.

To further probe the roughness characteristics of Bennu’s surface, we binned the OLA roughness proxy map into two groups (**Figure 14B**, where the boundary value is 0.12 m, the approximate mid-point of the first—and largest—bin of the roughness histograms, **Supplementary Figure 7**). This binned roughness map clearly identifies the rougher regions of the Rugged Unit. However, it also highlights regions in the Rugged Unit that are smoother than the global median (e.g., 130°E, 50°N, as well as the smooth lobate deposit ~270°E, 5°S) and regions in the Smooth Unit that are rougher than the global median (e.g., 90°E, 0°N). These small-scale roughness deviations correspond to, for example, a small collection of boulders

within the Smooth Unit that is not large enough in spatial scale (and/or lacks sufficiently distinct boundaries) to be part of the other geologic unit.

Other maps of surface roughness have also been derived from thermal modeling using data from the OSIRIS-REx spectrometers (Rozitis et al., 2020, see their Fig. 1C-D). These data are discussed in Section 6.5.

6.3 Normal albedo

Data from the MapCam imager of OCAMS have shown that the largest boulders on Bennu are darker than the average surface (average reflectance: 0.0439) (DellaGiustina et al., 2020); as such, we would expect that the Rugged Unit, which contains most of the large boulders, to have lower albedo than the Smooth Unit. A global normal albedo map from the PolyCam imager of OCAMS (Golish et al., 2021) (**Figure 15A**) shows that the Smooth Unit covers most of the highest-albedo portions of Bennu's overall dark surface (orange/yellow contours, e.g., centered near 60°E, 20°N; 340°E, 30°N). Additionally, the Rugged Unit includes all of the lowest-albedo regions (specifically where large scars are present, e.g., Roc Saxum ~25°E, 25°S; and Tlanuwa Regio ~260°E, 30°S).

However, not all portions of the Rugged Unit have low albedo, and likewise some localized regions in the Smooth Unit have low albedo. We credit this discrepancy to the heterogeneous reflectance properties of boulders on Bennu; boulders appear to belong to at least two populations, one with low reflectance (~0.034–0.049) and one with high reflectance (~0.049–0.074) (DellaGiustina et al., 2020). The Rugged Unit contains collections of boulders that may be mixtures of these two types, so the normal albedo anywhere in the Rugged Unit could vary depending on the relative proportions of these two groups. Likewise, a single low-reflectance boulder (or particles formed from the breakdown of low-reflectance boulders) present in the Smooth Unit could lower the albedo of an otherwise brighter region.

6.4 Thermal emission spectral characteristics

Hamilton et al. (2021) found that Type 2 OTEs spectra were indicative of thin dust coatings and spatially correlated very well with the distribution of large boulders on Bennu. We find that Type 2 spectra are therefore also well correlated with the Rugged Unit (**Figure 15B**). Hamilton et al. (2021) attribute the somewhat paradoxical spatial correlation of fine-grained dust and the largest boulders on Bennu to either the in-situ breakdown of the host boulders, or enhanced trapping of fine-grained dust on these boulders' surfaces.

We propose that the dust coatings on large boulders are related to mass movement and boulder excavation. DellaGiustina and Emery et al. (2019) first argued that the largest boulders were excavated from the subsurface by mass movement. Additionally, studies of crater morphology found that many small craters contained anomalously smooth interiors, leading Bierhaus et al. (2019) to propose that there is a near-surface layer of fine-grained material covered by a coarser, boulder-rich layer on the surface. If large boulders were exhumed from the subsurface, their dust coatings may represent trapped material originating from the fine-grained

near-surface layer. The fine-grained particles may remain trapped on these boulders if they were exhumed in the relatively recent past, and/or because these very large, low-reflectance boulders have a rough, hummocky surface texture that could trap dust more easily than their brighter, smoother counterparts (DellaGiustina et al., 2020; Jawin et al., 2020c).

6.5 Thermal inertia and thermal roughness

Global maps of thermal inertia based on OSIRIS-REx spectrometer data (Rozitis et al., 2020) identified a dominant equatorial feature in the data. The elevated thermal inertia in the equatorial region was attributed potentially to compaction, boulder maturation, or self-sorting of stronger, higher-thermal-inertia boulders as mass movement transports material towards the equator.

As discussed above, the geologic units do not show a strong equatorial trend or any spatial associations with the equatorial bulge or its boundary. The thermal inertia maps therefore do not show a spatial correlation with the geologic unit boundaries (**Supplementary Figure 8A**). This discrepancy is probably partly due to the different probing depth of the thermal data (upper few centimeters) relative to the visible images that are sensitive only to the surface. In addition to the different probing depths, we credit the lack of correlation in the geologic units with the thermal inertia data, as well as in other global datasets dominated by an equatorial feature, to the absence of any distinct morphologic contacts around the equatorial bulge.

The thermal analysis of Rozitis et al. (2020) derived thermal roughness maps along with the maps of thermal inertia. While the thermal inertia and thermal roughness maps were derived simultaneously, the resulting maps show distinct spatial relationships (compare **Figure 7A and 7B**). The thermal roughness maps show spatial variability very similar to those shown in the OLA roughness proxy maps (**Figure 14A**), with minimal evidence of the equatorial feature found in the thermal inertia map. Therefore, although there is an apparent lack of correlation between thermal inertia and geologic units, thermal roughness appears to be in accord with the geologic unit boundaries.

7. Relative unit ages

Because Bennu is a rubble-pile asteroid with a surface that shows signs of recent rearrangement, when we refer to “ages” of geologic units, we refer to the resurfacing age or the relative period of time that material has been exposed on the surface, rather than the absolute formation ages of the material present in those units. We investigate the ages of the two units below.

7.1 Relative ages from stratigraphy and mass movement features

Determining relative ages of the geologic units on Bennu is somewhat more difficult than for larger planetary bodies. The traditional method of establishing relative ages, through examining the stratigraphy at contacts between units, is only feasible in a few regions, namely where there are lineaments that coincide with unit boundaries (**Figure 12**). The most distinct

example of a contact enabling stratigraphic analysis is around Bennu's longest and most distinct scarp (lineament 3, **Table 1**, white arrow in **Figure 5**) that represents the boundary between the Smooth and Rugged Units (**Figure 12**). The Rugged Unit east of the scarp is depressed by ~10 m relative to the smoother surface west of the scarp (**Figure 6**) and is morphologically consistent with slope collapse or other mass wasting from the scarp, which would have required the pre-existing surface (the Smooth Unit) to have already been present. Therefore, the Rugged Unit probably incised into the Smooth Unit, so the Smooth Unit must be older than the Rugged Unit. The same stratigraphic relationships are also found at the other lineaments, where the Smooth Unit appears to have collapsed, forming a scarp that outlines the current edge of the Rugged Unit.

The inference that the Smooth Unit is older than the Rugged Unit can be further examined by studying the distribution of mass movement features. Jawin et al. (2020a) showed that mass movement features, predominantly in the form of small-scale creep, follow the current slope distribution, which changes over time as a result of spin period changes (Yarkovsky-O'Keefe-Radzievskii-Paddack, YORP, thermal torquing, e.g., Bottke et al., 2006). Therefore, this mass movement (yellow arrows, **Figure 12**) must have occurred in the recent past (~200 kyr), based on the observed acceleration in spin rate (Pergenther et al. 2019). As 85% of mass movement features are located in the Rugged Unit (**Table 4**), recent resurfacing appears to have been concentrated in the Rugged Unit, while the Smooth Unit has been experienced relatively less resurfacing over the same time period. This distribution supports the inference that the Smooth Unit is an older surface than the Rugged Unit.

7.2 Ages from the global crater distribution

Bierhaus et al. (2022) investigated the global crater population and the crater size-frequency distribution (SFD) of all mapped craters ($N = 1560$ craters) ranging in diameter from <1 m to over 200 m (green curve, **Figure 16**). They proposed crater retention ages for the surface of Bennu using a scaling relationship designed for rubble-pile surfaces (Tatsumi & Sugita, 2018). They found that the largest craters on Bennu (~100 m diameter) are well modeled by surface ages of 10–65 Myr using an impact flux in the Main Belt. In comparison, craters less than 2.3 m in diameter show a rapid decrease in number density and no longer follow a power-law trend. Bierhaus et al. (2022) refer to this turnover at small crater sizes as a “fishhook” in the differential SFD. They demonstrate that this depletion of small craters is not due to crater erasure (e.g., via seismic shaking or mass movement). Rather, the transition from the power-law trend into the fishhook shape indicates a transition from impact cratering into the bulk surface to impact armoring, where the impactor is of comparable size or smaller than the target particle (an individual boulder), resulting in a crater that is smaller than expected or does not form at all—instead, the boulder is disrupted (Tatsumi & Sugita, 2018). Using the armoring scaling relationship of Tatsumi & Sugita (2018), Bierhaus et al. (2022) modeled the crater retention age of the surface for the small craters (~tens of meters and smaller) and found that the smallest

modeled residuals occurred for ages between 1.6–2.2 Myr using an near-Earth space impactor flux.

To examine the relative ages of the two geologic units on Bennu, we studied the global crater distribution and compared differential SFDs of both units to the global distribution and ages from Bierhaus et al. (2022). The SFDs for the two geologic units (blue and orange curves, **Figure 16**) follow the same general trend as the global distribution (green curve): at large crater sizes (larger than ~50 m), the distributions are not distinguishable from the global distribution. Likewise, at smaller crater diameters, the distributions in both geologic units show the same fishhook shape as the global distribution, with a peak in the SFD at the same crater diameter, 2.3 m. These data suggest that impact armoring operates everywhere on the surface of Bennu to suppress the formation of craters smaller than ~3 m, regardless of the geologic unit.

Although both geologic units contain similarly shaped SFDs to the global distribution, the Smooth Unit contains more small craters (<20 m) than the Rugged Unit, leading to a vertical offset of the Smooth Unit crater distribution above the global distribution (orange curve, **Figure 16**). Reciprocally, a relative depletion of craters <20 m in the Rugged Unit causes its crater distribution to be vertically offset below the global distribution (blue curve, **Figure 16**). We do not credit the variable concentration of <20-m diameter craters to impact armoring alone—as demonstrated in Bierhaus et al. (2022), impact armoring results in a depletion of craters at diameters below a threshold where cratering in the bulk surface transitions to particle armoring. This depletion of craters below a given diameter would be evident in a differential SFD plot by a sudden drop in crater concentration (i.e., a fishhook shape), but would not lead to a wholesale vertical shift in the crater SFD, as is seen in the Rugged Unit at craters <20 m relative to the global distribution. Note that the interplay between the crater diameter corresponding to the fishhook peak (which can shift the peak in the SFD left or right on the plot) and the crater abundance corresponding to the vertical offset (shifting the distribution up or down) is complex and requires significant modeling to accurately detail (see methods of Bierhaus et al., 2022), but here the similarity in fishhook shape and location—despite the vertical offset—suggests the dominant difference between the rugged and Smooth Unit SFDs is due to crater retention age. Therefore, the depletion of craters <20 m in diameter is more likely due to a resurfacing event(s) that erased these small craters in the Rugged Unit more efficiently than in the Smooth Unit. One such resurfacing process is mass movement, which may have occurred more rapidly or efficiently in the Rugged Unit.

The crater distributions can provide insight into the ages of the two units relative to the global crater distribution. Bierhaus et al. (2022) found a crater retention age for the largest craters of 10–65 Myr; as the SFDs for both geologic units are indistinguishable (within error) from the global distribution at large crater sizes (~100 m diameter), both units may have initially formed (or had crater retention ages reset) during this same period.

For the population of craters smaller than ~100 m, Bierhaus et al. (2022) state that the number of craters in the peak of the small-crater distribution (i.e., the vertical position of the SFD peak at 2.3 m diameter) provides a unique constraint on the crater retention age at that

diameter. They found the global distribution of these small craters (peaking ~ 2.3 m) corresponded to an age of 1.6–2.2 Myr in near-Earth space. The Rugged Unit contains fewer craters < 20 m than the global distribution, shifting the SFD peak at 2.3 m diameter below the global distribution; the Rugged Unit therefore should have a younger crater retention age than the global population's age of ~ 2 Myr (in near-Earth space). In comparison, the Smooth Unit contains relatively more small craters than the global distribution, shifting the SFD peak above the global distribution—this suggests that the Smooth Unit may be older than the estimated ~ 2 Myr for the global distribution.

7.3 Ages from the distribution of fresh craters

Small craters are, in general, younger than large craters, and DellaGiustina et al. (2020) showed that spectral color can be used as a discriminator for age of craters on Bennu. They found that the reddest craters (redder than Bennu's blue average by 0.5σ or 1σ , where σ is the full-width at half maximum of the global distribution of b' to x spectral slopes) are the freshest craters on Bennu. These fresh craters are also small, less than ~ 20 m diameter, the same size range over which we found a depletion of craters in the Rugged Unit in the section above. Note that not all small craters (< 20 m) are redder than average, although all redder-than-average craters are small.

We found that these fresh craters are not evenly distributed across the Smooth and Rugged Units (**Figure 17**). Of the 79 freshest craters (redder than Bennu's average surface by at least 1σ), the Smooth Unit contains 67% (53 craters), compared to the Rugged Unit's 33% (26 craters) (**Table 6**). In a slightly larger population of the 255 craters redder than Bennu's average surface by at least 0.5σ , the Smooth Unit contains 71% (182 craters). When scaled for surface area, the Smooth Unit contains a factor of ~ 3 more fresh craters than the Rugged Unit (in both populations of craters 1σ and 0.5σ redder than average).

DellaGiustina et al. (2020) found that the freshest craters (redder by at least 1σ , 79 craters) could have formed within the past ~ 100 kyr. Given that we also investigated the broader population of fresh craters (redder by at least 0.5σ , 255 craters) from DellaGiustina et al. (2020), we assumed a slightly older formation age of ~ 500 kyr; this age was derived by using a production function with the same slope fit to the largest of the 0.5σ craters. This predicts ~ 5 times more 10-m craters and would require 5 times longer, thereby leading to a ~ 500 -kyr production age (**Supplementary Figure 9**).

Differences in the distribution of the freshest craters imply that resurfacing has occurred during approximately the same period as the formation of those craters. If, for example, resurfacing occurred and concluded everywhere on Bennu more than ~ 500 kyr ago, fresh craters would be uniformly distributed across the surface. Because the Rugged Unit contains fewer fresh craters by a factor of ~ 3 than the Smooth Unit, at least a portion of resurfacing in the Rugged Unit must have occurred within the past ~ 100 – 500 kyr. This observation agrees with surface age from the mass movement analysis of Jawin et al. (2020a), suggesting small-scale creep on Bennu was concentrated in the Rugged Unit in the past ~ 200 kyr. Creep has likely also operated in the

Smooth Unit, but it must have been insufficient to erase as many small fresh craters. These findings are also consistent with the analysis of the global crater SFD, where the Rugged Unit has a small-crater (<20 m) retention age of less than ~2 Myr, while the Smooth Unit has a small-crater retention age of greater than ~2 Myr. Therefore, we conclude that the Rugged Unit is younger than the Smooth Unit as it has been at least partly resurfaced within the past ~500 kyr.

A potential caveat in the age analyses from the crater distributions is that impact armoring may play a larger role than anticipated, and may account for the depletion in craters <20 m in the Rugged Unit seen in both the global crater distribution and the fresh crater distribution. However, there is still substantial morphologic evidence that the Rugged Unit has a younger resurfacing age than the Smooth Unit, specifically the stratigraphic contacts discussed in Section 7.1, and the concentration of mass movement features in the Rugged Unit, which formed within the past ~200 kyr.

8. Bennu's chronologic history

In this section, we bring together our results with previous studies to reconstruct a complete geologic timeline for Bennu (**Figure 18**), including possible formation and evolutionary pathways for the two geologic units.

8.1 Formation of Bennu materials

Bennu is expected to be as old as ~4 billion years (Bottke et al., 2015; 2020), although its crater retention age may actually be much younger, ~10–65 Myr (Bierhaus et al., 2022). During its lifetime, the anticipated impact energies on Bennu (both during its time in the Main Belt and in NEA space) were insufficient to produce impact brecciation and lithification (DellaGiustina and Emery et al., 2019). Therefore, the constituent particles on Bennu should pre-date the existence of the rubble pile, and are expected to have formed on the parent body asteroid (with the exception of a minor component of exogenous particles that were likely sourced from Vesta, DellaGiustina et al., 2021). Bennu's parent body likely originated from the New Polana or Eulalia families in the inner Main Belt (~2.4–2.49 AU) (Bottke et al., 2015).

This parent body must have experienced extensive aqueous alteration in order to form the ubiquitous phyllosilicates found on Bennu (Hamilton et al., 2019). Additionally, the discovery of centimeters-thick carbonate-bearing veins in Bennu's boulders (Kaplan et al., 2020) implicate large-scale, open-system fluid flow and hydrothermal alteration on the parent body that lasted thousands to millions of years. Aqueous activity must have occurred in the early period of the Solar System, and within a few million years after accretion (e.g., Cohen and Coker, 2000; Bland and Travis, 2017), during which time there was an active heat source in the parent body due to the decay of short-lived radionuclides. Lithification may not yet have occurred at this point in the parent body—rather, the body could have resembled a “convecting mudball” (Bland and Travis, 2017) within which aqueous alteration and hydrothermal deposition occurred. Lithification appears to have preserved heterogeneity of the parent body within the boulder population, as several studies have found differences in the color, thermomechanical, and morphologic

properties of boulders (e.g., DellaGiustina et al., 2020; Jawin et al., 2020c; Rozitis et al., 2020). When the parent body was disrupted, these heterogeneous fragments were incorporated into Bennu. Analyses of the returned sample will undoubtedly clarify the alteration and lithification history of the parent body.

8.2 Bennu in the Main Belt (>2 Myr ago)

Several analyses have demonstrated that Bennu transitioned from its original orbit in the Main Belt to near-Earth space ~2 Myr ago (1.75 Myr, Ballouz et al., 2020; 1.6 – 2.2 Myr, Bierhaus et al., 2022; 2.6 Myr, Bottke et al., 2015). This inward migration through the Main Belt was driven by the Yarkovsky effect (Bottke et al., 2015; Chesley et al., 2014; Farnocchia et al., 2021). The anticipated dynamical, thermal, and impact environments in the Main Belt are different than those in the inner Solar System, so disentangling activity that occurred prior to 2 Myr ago is of scientific interest. While much of Bennu's surface may have experienced resurfacing to some degree during its time as an NEA over the past 2 Myr, certain geologic features likely have been preserved from their original formation in the Main Belt.

Formation of shape features. Bennu's equatorial bulge is an old geologic feature as evinced by its concentration of large superposing craters (Walsh et al., 2019). Analyses of the global crater distribution (Bierhaus et al., 2022) show that the large craters on Bennu could have formed within the last few tens of millions of years, so the bulge must be older than at least ~10 Myr. Models of bulge formation vary and predict different formation ages for the bulge: it could be an original feature, forming upon reaccumulation (Michel and Ballouz et al., 2020); or an evolved feature, forming via internal deformation (Hirabayashi et al., 2019) or surficial mass flow (e.g., Walsh et al., 2008). Any of these models for bulge formation are consistent with the old age of the bulge, if it formed at least ~10 Myr ago—although bulge formation upon reaccumulation would imply a much older age if Bennu is linked to the Eulalia or New Polana asteroid families (Bottke et al., 2015). The high-standing and low-lying regions also probably formed at a similar time in Bennu's history as the equatorial bulge, as evinced by similarly high crater densities and subdued morphology (e.g., Barnouin et al., 2019), but as no distinct boundaries exist on the high-standing regions, low-lying regions, or equatorial bulge, it is not possible to determine their relative stratigraphic ages. Models of high-standing region formation include internal deformation by “wedging” rotational failure during a period of spin-up early in Bennu's history (Barnouin et al., 2019; M. G. Daly et al., 2020); other models propose that large boulders in the interior may have shifted early in Bennu's history, leading to the formation of large ridges (Zhang et al., 2020).

Formation of large craters. Cratering is an ongoing process, but the formation and modification of several large craters have particularly shaped the evolution of Bennu's surface. The craters preserved on Bennu's surface post-dated the initial formation of the shape features, as craters superpose the equatorial bulge and high-standing/low-lying regions. Several large (~50 to 100 m) craters are present on the boundaries of high-standing and low-lying regions and appear to have altered the boundaries of these shape features. For example, the large craters

located at $\sim 60^\circ\text{E}$, 60°N (**Figure 5**) and 160°E , 30°N contain crater rims that correspond to boundaries of the high-standing and low-lying regions.

The largest crater we mapped on Bennu (Minokawa Crater) contains the largest mass flow (smooth lobate deposit) and is located to the east of the longest lineament on Bennu (lineament 3, **Table 1**). The crater is stratigraphically older than this mass flow, which likely originated at the lineament. It is possible that the formation of the crater triggered the slope collapse that led to the formation of the scarp and mass flow, via seismic shaking and/or ejecta interaction with the surrounding region. If this slope collapse and mass flow were triggered by the impact (while in the Main Belt), it would represent the oldest identifiable mass movement feature on Bennu.

A second large crater (Bralgah Crater, centered $\sim 324^\circ\text{E}$, 43°S , ~ 70 m diameter) has been found associated with the only large-scale ejecta deposit on Bennu (Perry et al., in review), which is distinct because it is the largest photometrically distinct and smooth area on Bennu. The ejecta deposit is associated with a larger smooth region to the north, argued to be a flow field induced by interactions of ejecta with the surrounding terrain. While Perry et al. (in review) argue that Bralgah Crater is relatively young—due to the preservation of the crater and the flow field—it is in a similar size range (~ 50 to 100 m diameter) to the largest craters on Bennu, which Bierhaus et al. (2022) found were best modeled by an impact flux in the Main Belt. Therefore, Bralgah Crater probably formed while Bennu was still in the Main Belt, ~ 2 Myr ago or earlier.

Formation of the Smooth and Rugged Unit surfaces. Bierhaus et al. (2022) demonstrated that Bennu's crater retention age for the largest craters (~ 100 m) is 10–65 Myr, while Bennu was in the Main Belt. As shown in **Figure 16**, differential crater SFDs for the smooth and Rugged Units are not distinguishable from the global distribution at these large crater sizes—so both units were probably formed (or substantially resurfaced) during this time period (10–65 Myr ago) in the Main Belt.

The small-crater (<20 m) SFD suggests the Rugged Unit has experienced resurfacing within the past few hundred thousand years (discussed in the following section), while the Smooth Unit may not have been significantly resurfaced for over the past 2 Myr—this interpretation suggests that the Smooth Unit has been well preserved from its formation in the Main Belt. This interpretation does not imply that no resurfacing has occurred in the Smooth Unit while Bennu has been an NEA, but rather that resurfacing has been insufficient to erase small (<20 m) craters. The Smooth Unit may therefore most closely resemble the surface of Bennu as it appeared in the Main Belt.

How did the Smooth Unit form? The smooth surface associated with Bralgah Crater (Perry et al., in review), as well as the smooth lobate deposit inside Minokawa Crater, show that smooth surfaces can form in association with large craters. Since impacts were probably the dominant resurfacing process acting in the Main Belt, Bennu's surface could have been extensively altered by impact-induced slope failure and/or ejecta interactions in the Main Belt which formed smooth surfaces that are now preserved in the Smooth Unit. Note that the original surface in the Rugged Unit probably also formed at the same time as the Smooth Unit (based on

the SFD of large craters, ~100 m) due to the same impact-induced surface activity, and may have initially been smoother (but, unlike the Smooth Unit, the Rugged Unit subsequently experienced more extensive resurfacing).

8.3 Transition to near-Earth space

At ~2 Myr ago, Bennu was ejected out of the Main Belt and transitioned to an NEA. This age is supported by recent work of Bierhaus et al. (2022) studying the global crater distribution, Ballouz et al. (2020) identifying small craters hosted on boulders, and Bottke et al. (2015) performing dynamical simulations incorporating the coupled Yarkovsky/YORP effects. Bennu's transition to near-Earth space brought it ~2.5 times closer to the Sun, which would have changed the thermal environment, sped up the efficiency of YORP effects by ~10 times (as this process is affected by distance from the sun squared) (Bottke et al., 2006), and decreased the impact flux by ~50 times (Ballouz et al., 2020). So the nature of surface evolution after the transition would have changed (in general) from dominantly impact-related modification to YORP-driven mass movement and other thermal effects such as thermal fracturing of boulders (Molaro et al., 2020; Delbo et al., 2022)—although impacts still play a role in surface modification in near-Earth space.

Resurfacing in the Rugged Unit. Although the Rugged Unit was initially formed in the Main Belt, resurfacing within the past ~2 Myr has erased small craters (<20 m) more rapidly than in the Smooth Unit. If mass movement is the dominant process by which this resurfacing and crater erasure occurred, then the rugged surface texture (which distinguishes it from the Smooth Unit) probably also started to develop soon after Bennu transitioned to near-Earth space. Continuous small-scale surface creep probably operated constantly over the last 2 Myr in response to YORP cycles, which would have transported material (probably relatively fine-grained material) towards the equatorial region (e.g., Jawin et al., 2020a). Saxa in the mid-latitudes were excavated from the sub-surface by the transport of up to ~10 m of material towards the equator (Jawin et al., 2020a)—these saxa are concentrated in the Rugged Unit (**Figure 12**). Larger, less frequent mass movement events would also have led to the formation of the scarp-type lineaments (**Figure 5**) and associated boulder-rich regions. Other large-scale mass movement events may have occurred that have since been modified or erased and no longer have distinct boundaries.

8.4 Surface evolution within last ~500 kyr

Bennu's surface has been modified in the past half million years by impacts and mass movement, which developed the surface texture and extent of the Rugged Unit. Impact craters have continued to form across Bennu over the past ~500 kyr, forming small (<20 m) craters redder than Bennu's average color (DellaGiustina et al., 2020)—although impact armoring has suppressed the formation of small craters (<3 m) across the surface (Bierhaus et al., 2022). The Rugged Unit contains fewer small (<20 m diameter, **Figure 16**) and fresh (**Figure 17**) craters than the Smooth Unit, which we credit to small-scale surface creep that is concentrated in the

Rugged Unit (**Figure 12**) and occurred within the past ~ 200 kyr (Jawin et al., 2020). Jawin et al. (2020a) found that the removal ~ 10 m of material was required to exhume the largest mid-latitude boulders from the subsurface via mass movement, but only a fraction of this depth would have been transported during the past ~ 200 kyr. We assume, conservatively, that the mass movement features formed via small-scale creep over the past 200 kyr (yellow arrows, **Figure 12**) account for the transport of $\sim 1\text{--}2$ m of material towards the equator. If we consider the capacity for crater erasure via this surface creep, the removal of a layer 1–2 m thick could erase craters less than ~ 20 m, assuming a depth-to-diameter ratio of ~ 0.1 (R. T. Daly et al., 2020).

The mass movement that excavated saxa may also have developed the rugged surface texture by preferentially removing smaller particles and transporting them towards the equatorial region. Small particles, mobilized by mass movement, could also have been removed from the surface either by percolation into Bennu's interior (as the macroporosity of the body is substantial, $\sim 50\%$, Barnouin et al., 2019) or by lofting off the body if they were sufficiently accelerated to reach escape velocity. The transport or removal of fine particulates due to mass movement would increase the average particle size, and the surface roughness, over time.

Regions where mass movement was enhanced, such as those with steep slopes, would have determined the locations where the Rugged Unit developed. The mid-latitudes currently have the steepest slopes on Bennu ($\sim 18^\circ$, Scheeres et al., 2019), and are largely covered by the Rugged Unit. The boundaries of the Rugged Unit at $\sim 70^\circ\text{N/S}$ latitude correspond to these steep-sloped mid-latitude regions, and saxa in several locations (primarily in the southern mid-latitudes) are located at or near this latitudinal boundary (**Figure 12**); these saxa may be retaining material on their upslope sides, while downslope material (on the equator-facing sides) is free to migrate towards the equator (M. G. Daly et al., 2020; Barnouin et al., 2022). The equatorial migration of material could have developed the N-S orientation seen in the geologic units (**Figure 10**). Therefore the surface texture, distribution, orientation, and concentration (or relative paucity) of saxa (and craters) can be explained by mass movement over at least the past several hundred thousand years. These properties, as well as a summary of properties of the Smooth Unit, are summarized in a Description of Map Units in **Table 7**.

8.5 Present-day surface activity

The era of OSIRIS-REx observations over the past three years has been characterized by several particle ejection events off the surface of varying magnitude. OSIRIS-REx observed numerous PE events, but as no resolvable surface change has been detected at their source regions, it is unclear how common these events were in earlier periods of Bennu's history, and whether larger prior events (if they occurred) would be resolvable on the surface.

Even more recently, the surface of Bennu was modified, at least locally, due to the OSIRIS-REx sample collection event at the Nightingale sample site (Lauretta & OSIRIS-REx TAG Team, 2021). Subsequent analyses will reveal the magnitude of the change on Bennu's surface.

While no visible surface change has been documented during the OSIRIS-REx mission (except for the sample collection at Nightingale), surface activity is expected to continue in the near future, including particle ejection events, formation of small craters, and creep-style mass movement as YORP-induced spin period changes alter the global geopotential.

9. Geologic context of the sample site

The sample site, Nightingale, is located in a crater 20 m in diameter (Hokioi crater) that is situated within a large crater ~120 m in diameter, both of which are located within the Smooth Unit (**Figure 12**). Although the Smooth Unit is older as a whole than the Rugged Unit, we are confident that recently exposed material was sampled. The regional geologic setting of Nightingale in the high mid-latitudes (56°N) is characterized by steep slopes (~35°) (Scheeres et al., 2019) that are susceptible to mass movement towards the south. In addition, Hokioi crater is reddest (Rizos et al., 2021), and therefore one of the youngest craters on Bennu (DellaGiustina et al., 2020). So despite our interpretation that the Smooth Unit is older than the Rugged Unit, it is expected that the Nightingale site itself (and therefore the returned sample) contains fresh, relatively recently exposed material.

The probable youthfulness of the Nightingale sample site also highlights the broader point that, although we establish approximate ages for the Smooth and Rugged Units, it is not necessarily required that all materials within the unit must be of the same age. The global assessments we provide here are useful for establishing broad-scale analyses and comparisons, but small-scale trends may show more complex temporal relationships. To further probe the detailed temporal relationships of the Nightingale sample site and surrounding regions, landing site-scale mapping is required.

10. Comparison with the geologic evolution of Ryugu

Rubble-pile asteroid (162173) Ryugu shares many physical similarities with Bennu, such as a spinning-top shape, boulder-rich surface, near-Earth orbit, and similar sizes, so we compare our mapping results to a preliminary global geologic map of Ryugu (Miyamoto et al., 2019). Unlike on Bennu, where the equatorial bulge does not seem to have greatly affected the formation of geologic units, material appears to be migrating away from the equatorial ridge on Ryugu, Ryujin Dorsum, towards the mid-latitudes (the current global geopotential minimum on Ryugu) (Miyamoto et al., 2019). The equatorial ridges on both asteroids formed relatively early in their histories, as evidenced by their higher densities of superposed craters, with the exception of the equatorial region on the western bulge of Ryugu (Hirata et al., 2020) which may have been more recently modified (e.g., Hirabayashi et al., 2019). The equatorial ridge on Ryugu is also more pronounced than the equatorial bulge on Bennu. This distinction is probably at least partly due to variable spin periods on the two asteroids: Bennu is currently in a period of spin-up (current spin period: 4.3 hr, Lauretta and DellaGiustina et al., 2019), which defines the equatorial region as the global geopotential minimum, and as such material is migrating towards the

equator. Ryugu, in contrast, is in a spin-down period (current spin period: 7.6 hr, Watanabe et al., 2019), and the mid-latitudes are the location of the global geopotential minimum.

Equatorial ridge formation on Ryugu was followed by the formation of large craters and troughs (Horai and Tokyo Fossae) (Miyamoto et al., 2019). Benu's high-standing and low-lying regions are geologically old features, of similar age to the equatorial bulge (although we could not determine the relative ages of these features, so it is unclear whether the bulge is older than the high-standing and low-lying regions). Similarly, the high-standing and low-lying regions on Benu were shaped in part by the formation of large craters.

The global geologic map of Ryugu contains at least two units that are distinguishable by a variable number density of boulders and variations in brightness and color (Sugita et al., 2019). This is very similar to our global geologic map of Benu, which contains two geologic units defined by a variable surface texture that is a function of boulder concentration, which corresponds to variations in normal albedo. We also find that other datasets are complementary to our geologic units, including slope, surface roughness, albedo, and thermal emission spectral characteristics.

These comparisons illustrate how the irregular, boulder-rich surfaces of rubble-pile asteroids cannot be characterized (from a global perspective) based on the properties of any individual boulder. Rather, regional-scale units are differentiated by local accumulations of boulders determined by the spin state and geopotential. The specific characteristics of boulders on a given rubble pile (reflectance, strength, composition, texture) determine the specific properties of the surface, including its characteristic particle size, reflectance, and color properties, and the initial distribution of boulders on (and inside) the body may determine how the boulder population evolves. Finally, the changing surface dynamics of a rubble pile may be critical in considering its surface evolution, including its age, spin period, duration in the Main Belt, and its time as an NEA. Further analyses dedicated to comparing global geologic properties of Benu and Ryugu (and other rubble-pile asteroids) are required to better understand the evolution of these bodies.

11. Conclusions

With our global geologic map of Benu (**Figure 12**), we classified the entire surface into two geologic units based on input maps of surface texture, geologic features, and shape features. Several eras of geologic activity are evident in observations of Benu: (1) the formation of its constituent materials, which it inherited from its parent body; (2) the earliest period of its evolution where the shape features (equatorial bulge, high-standing regions, and low-lying regions) likely formed; (3) its lifetime in the Main Belt, dominated by the formation of large impact craters and the surfaces of the Smooth and Rugged Unit; (4) its transition to near-Earth space and the initial resurfacing in the Rugged Unit ~ 2 Myr ago; and (5) Benu's recent surface evolution in the past 500 kyr, including the formation of small craters (although the smallest craters, < 3 m, have been suppressed due to impact armoring) and equatorial mass movement concentrated in the Rugged Unit. We determined, based on stratigraphy and the distribution of

geologic features, that the Rugged Unit is younger than the Smooth Unit and has been resurfaced within the past ~0.5 Myr, while the Smooth Unit has not been significantly resurfaced within the past ~2 Myr and therefore may resemble the surface when Bennu was in the Main Belt. However, it is important to note that Bennu is a rubble pile, and therefore the “younger” and “older” regions of the surface only refer to their resurfacing histories, and not to the ages of the individual boulders.

The return of the OSIRIS-REx sample in September 2023 will enable us to establish various ages for the rocks on Bennu, including formation ages, alteration ages, shock ages, and exposure ages. Each of these distinct ages can provide absolute chronologies for the relative chronologies we proposed above in **Section 8**. Mapping of the Nightingale sample site will provide additional insights into the relationship between the returned sample and Bennu’s evolutionary history.

Acknowledgments: We thank David Williams and Jennifer Scully for their feedback on the manuscript. We also thank Lillian Ostrach for productive conversations about mapping methodology. We are grateful to the entire OSIRIS-REx team for making the encounter with Bennu possible. This material is supported by NASA Contract NNM10AA11C through the New Frontiers Program. M. Pajola was supported by the Italian Space Agency under ASI-INAF agreement no. 2022-1-HH.0.

Data availability statement: All image and topographic data used in this analysis are available in the PDS (<https://sbn.psi.edu/pds/resource/orex/>), the SBMT (<http://sbmt.jhuapl.edu/>), and/or have been previously published. The locations of all geologic features were included in the text or (for larger datasets) are available on FigShare (Jawin et al., 2022a,b). All SBMT shapefiles generated as part of this work are available on FigShare (Jawin et al., 2022c).

References

- Ballouz, R.L., Walsh, K.J., Barnouin, O.S. et al. (2020). Bennu’s near-Earth lifetime of 1.75 million years inferred from craters on its boulders. *Nature*, 587, 205–209. <https://doi.org/10.1038/s41586-020-2846-z>
- Bland, P. A., & Travis, B. J. (2017). Giant convecting mud balls of the early solar system. *Science Advances*, 3(7), e1602514. <https://doi.org/10.1126/sciadv.1602514>
- Barnouin, O. S., Daly, M. G., Palmer, E. E., Gaskell, R. W., Weirich, J. R., Johnson, C. L., et al. (2019). Shape of (101955) Bennu indicative of a rubble pile with internal stiffness. *Nature Geoscience*, 12(4), 247–252. <https://doi.org/10.1038/s41561-019-0330-x>
- Barnouin, O. S., Daly, M. G., Palmer, E. E., Johnson, C. L., Gaskell, R. W., Al Asad, M., et al. (2020). Digital terrain mapping by the OSIRIS-REx mission. *Planetary and Space Science*, 180, 104764. <https://doi.org/10.1016/j.pss.2019.104764>
- Barnouin et al. (2022). The Formation of Terraces on Asteroid (101955) Bennu, *JGR Planets*, *accepted*.
- Bennett, C. A., DellaGiustina, D. N., Becker, K. J., Becker, T. L., Edmundson, K. L., Golish, D. R., et al. (2021). A high-resolution global basemap of (101955) Bennu. *Icarus*, 357, 113690. <https://doi.org/10.1016/j.icarus.2020.113690>

- Bierhaus, E. B., Barnouin, O., McCoy, T. J., Connolly, H. C., Jawin, E., Walsh, K. J., et al. (2019). Asteroid (101955) Benu's Crater Population: Morphologies, Size-Frequency Distribution, and Consequences for Surface Age(s), *50*, 2496. Presented at the Lunar and Planetary Science Conference.
- Bierhaus, E. B., et al. (2022). Crater size-frequency distribution on Benu indicates impact armoring and young surface, *Nature Geoscience*, *accepted*.
<https://doi.org/10.1038/s41561-022-00914-5>
- Bottke, W. F., Vokrouhlický, D., Rubincam, D. P., & Nesvorný, D. (2006). THE YARKOVSKY AND YORP EFFECTS: Implications for Asteroid Dynamics. *Annual Review of Earth and Planetary Sciences*, *34*(1), 157–191.
<https://doi.org/10.1146/annurev.earth.34.031405.125154>
- Bottke, W. F., Vokrouhlický, D., Walsh, K. J., Delbo, M., Michel, P., Lauretta, D. S., et al. (2015). In search of the source of asteroid (101955) Benu: Applications of the stochastic YORP model. *Icarus*, *247*, 191–217. <https://doi.org/10.1016/j.icarus.2014.09.046>
- Bottke, W. F., D. Vokrouhlicky, R.-L. Ballouz, O. S. Barnouin, H. C. Connolly Jr., C. Elder, M. Marchi, T. J. McCoy, P. Michel, M. C. Nolan et al. (2020). Interpreting the Cratering Histories of Benu, Ryugu, and Other Spacecraft-explored Asteroids. *The Astrophysical Journal*, *160*, 14. <https://doi.org/10.3847/1538-4381/ab88d3>
- Cheng, A.F. et al., 2007. Fundamentally distinct outcomes of asteroid collisional evolution: Itokawa and Eros. *Geophys. Res. Lett.*, *34*(9), p.L09201.
- Cheng, A. F., Rivkin, A. S., Michel, P., Atchison, J., Barnouin, O., Benner, L., et al. (2018). AIDA DART asteroid deflection test: Planetary defense and science objectives. *Planetary and Space Science*, *157*, 104–115. <https://doi.org/10.1016/j.pss.2018.02.015>
- Chesley, S. R., Farnocchia, D., Nolan, M. C., Vokrouhlický, D., Chodas, P. W., Milani, A., et al. (2014). Orbit and bulk density of the OSIRIS-REx target Asteroid (101955) Benu. *Icarus*, *235*, 5–22. <https://doi.org/10.1016/j.icarus.2014.02.020>
- Christensen, P.R. et al. (2018). The OSIRIS-REx Thermal Emission Spectrometer (OTES) Instrument. *Space Sci. Rev.* *214*, 87.
- Cohen, B.A., and Coker, R.F., 2000, Modeling of liquid water on CM meteorite parent bodies and implications for amino acid racemization: *Icarus*, v. 145, p. 369-381, doi:10.1006/icar.1999.5229.
- Daly, M.G. et al. (2017). The OSIRIS-REx Laser Altimeter (OLA) Investigation and Instrument. *Space Sci. Rev.* *212*, 899–924. <https://doi.org/10.1007/s11214-017-0375-3>
- Daly, M. G., Barnouin, O. S., Seabrook, J. A., Roberts, J., Dickinson, C., Walsh, K. J., et al. (2020). Hemispherical differences in the shape and topography of asteroid (101955) Benu. *Science Advances*, *6*(41), eabd3649. <https://doi.org/10.1126/sciadv.abd3649>
- Daly, R. T., Bierhaus, E. B., Barnouin, O. S., Daly, M. G., Seabrook, J. A., Roberts, J. H., et al. (2020). The Morphometry of Impact Craters on Benu. *Geophysical Research Letters*, *47*(24), e2020GL089672. <https://doi.org/10.1029/2020GL089672>
- Delbo, M., K. J. Walsh, C. Matonti, J. Wilkerson, M. Pajola, M. Al Asad, C. Avdellidou, R.-L. Ballouz, C. Bennett, H. C. Connolly, D. DellaGiustina, D. Golish, S. Schwartz, D. S. Lauretta (2022), Rapid asteroid surface evolution as indicated by fracture alignment on Benu's rocks, *Nature Geoscience*, *accepted*.
- DellaGiustina, D. N., Emery, J. P., Golish, D. R., Rozitis, B., Bennett, C. A., Burke, K. N., et al. (2019). Properties of rubble-pile asteroid (101955) Benu from OSIRIS-REx imaging

- and thermal analysis. *Nature Astronomy*, 3(4), 341–351. <https://doi.org/10.1038/s41550-019-0731-1>
- DellaGiustina, D. N., Burke, K. N., Walsh, K. J., Smith, P. H., Golish, D. R., Bierhaus, E. B., et al. (2020). Variations in color and reflectance on the surface of asteroid (101955) Bennu. *Science*. <https://doi.org/10.1126/science.abc3660>
- DellaGiustina, D. N., Kaplan, H. H., Simon, A. A., Bottke, W. F., Avdellidou, C., Delbo, M., et al. (2021). Exogenic basalt on asteroid (101955) Bennu. *Nature Astronomy*, 1–8. <https://doi.org/10.1038/s41550-020-1195-z>
- El-Maarry, M. R., Thomas, N., Giacomini, L., Massironi, M., Pajola, M., Marschall, R., et al. (2015). Regional surface morphology of comet 67P/Churyumov-Gerasimenko from Rosetta/OSIRIS images. *Astronomy & Astrophysics*, 583, A26. <https://doi.org/10.1051/0004-6361/201525723>
- El-Maarry, M. R., Thomas, N., Gracia-Berná, A., Pajola, M., Lee, J. C., Massironi, M., et al. (2016). Regional surface morphology of comet 67P/Churyumov-Gerasimenko from Rosetta/OSIRIS images: The southern hemisphere. *Astronomy & Astrophysics*, 593, A110. <https://doi.org/10.1051/0004-6361/201628634>
- Ernst, C. M., Barnouin, O. S., Daly, R. T., & Small Body Mapping Tool Team. (2018). The Small Body Mapping Tool (SBMT) for Accessing, Visualizing, and Analyzing Spacecraft Data in Three Dimensions, 49, 1043. Presented at the Lunar and Planetary Science Conference.
- Farnocchia et al., (2021). Ephemeris and hazard assessment for near-Earth asteroid (101955) Bennu based on OSIRIS-REx data. *J. Icarus*. Icarus doi:10.1016/j.icarus.2021.114594
- Giacomini, L., Massironi, M., El-Maarry, M. R., Penasa, L., Pajola, M., Thomas, N., et al. (2016). Geologic mapping of the Comet 67P/Churyumov-Gerasimenko's Northern hemisphere. *Monthly Notices of the Royal Astronomical Society*, 462(Suppl_1), S352–S367. <https://doi.org/10.1093/mnras/stw2848>
- Golish, D.R. et al. (2020). Ground and In Flight Calibration of the OSIRIS-REx Camera Suite. *Space Sci. Rev.* 216, 12. <https://doi.org/10.1007/s11214-019-0626-6>
- Golish, D. R., Shultz, N. K., Becker, T. L., Becker, K. J., Edmundson, K. L., DellaGiustina, D. N., et al. (2021). A high-resolution normal albedo map of asteroid (101955) Bennu. *Icarus*, 355, 114132. <https://doi.org/10.1016/j.icarus.2020.114133>
- Hamilton, V. E., Simon, A. A., Christensen, P. R., Reuter, D. C., Clark, B. E., Barucci, M. A., et al. (2019). Evidence for widespread hydrated minerals on asteroid (101955) Bennu. *Nature Astronomy*, 3(4), 332–340. <https://doi.org/10.1038/s41550-019-0722-2>
- Hamilton, V. E., P. R. Christensen, H. H. Kaplan, C. W. Haberle, A. D. Rogers, T. D. Glotch, L. B. Breitenfeld, C. A. Goodrich, D. L. Schrader, T. J. McCoy, C. Lantz, R. D. Hanna, A. A. Simon, J. R. Brucato, B. E. Clark, and D. S. Lauretta (2021), Evidence for limited compositional and particle size variation on asteroid (101955) Bennu from thermal infrared spectroscopy, *Astronomy & Astrophysics*, accepted.
- Hergenrother, C. W., Maleszewski, C., Li, J.-Y., Pajola, M., Chesley, S. R., French, A. S., et al. (2020). Photometry of Particles Ejected From Active Asteroid (101955) Bennu. *Journal of Geophysical Research: Planets*, 125(9), e2020JE006381. <https://doi.org/10.1029/2020JE006381>
- Hirabayashi, M., Tatsumi, E., Miyamoto, H., Komatsu, G., Sugita, S., Watanabe, S., et al. (2019). The western bulge of 162173 Ryugu formed as a result of a rotationally driven

- deformation process. *Astrophysical Journal Letters*, 874(1), L10.
<https://doi.org/10.3847/2041-8213/ab0e8b>
- Hirata, N., Morota, T., Cho, Y., Kanamaru, M., Watanabe, S., Sugita, S., et al. (2020). The spatial distribution of impact craters on Ryugu. *Icarus*, 338, 113527.
<https://doi.org/10.1016/j.icarus.2019.113527>
- Jawin, E. R., Walsh, K. J., Barnouin, O. S., McCoy, T. J., Ballouz, R.-L., DellaGiustina, D. N., et al. (2020a). Global Patterns of Recent Mass Movement on Asteroid (101955) Benu. *Journal of Geophysical Research: Planets*, 125(9), e2020JE006475.
<https://doi.org/10.1029/2020JE006475>
- Jawin, E. R., Walsh, K. J., Barnouin, O. S., McCoy, T. J., Ballouz, R.-L., DellaGiustina, D. N., et al. (2020b). Instances of mass movement morphologies on Benu. Figshare.
<https://doi.org/10.6084/m9.figshare.12354773>
- Jawin, E. R., Walsh, K. J., McCoy, T. J., Connolly, H. C., Ryan, A. J., Ballouz, R. L., et al. (2020c). The Geology of (101955) Benu from the First Year of OSIRIS-REx Observations: Diverse Boulders and Recent Mass Movement. In *51st Lunar and Planetary Science Conference* (p. Abs. 1201). The Woodlands, TX.
- Jawin, E. R., et al., (2022a). Locations of mapped craters on Benu. Figshare.
 DOI:10.6084/m9.figshare.15911940
- Jawin, E. R., et al., (2022b). Locations of mapped saxes on Benu. Figshare.
 DOI:10.6084/m9.figshare.15911970
- Jawin, E. R., et al., (2022c). SBMT structure files for mapped geologic features on Benu. Figshare. DOI:10.6084/m9.figshare.15912036
- Kaplan, H. H., Lauretta, D. S., Simon, A. A., Hamilton, V. E., DellaGiustina, D. N., Golish, D. R., et al. (2020). Bright carbonate veins on asteroid (101955) Benu: Implications for aqueous alteration history. *Science*. <https://doi.org/10.1126/science.abc3557>
- Lauretta, D. S., Hergenrother, C. W., Chesley, S. R., Leonard, J. M., Pelgrift, J. Y., Adam, C. D., et al. (2019). Episodes of particle ejection from the surface of the active asteroid (101955) Benu. *Science*, 366(6470). <https://doi.org/10.1126/science.aay3544>
- Lauretta, D. S., DellaGiustina, D. N., Bennett, C. A., Golish, D. R., Becker, K. J., Balram-Knutson, S. S., et al. (2019). The unexpected surface of asteroid (101955) Benu. *Nature*, 568(7750), 55–60. <https://doi.org/10.1038/s41586-019-1033-6>
- Lauretta, D. S., and the OSIRIS-REx TAG Team (2021). The OSIRIS-REx Touch-And-Go sample acquisition event and implications for the nature of the returned sample. *52nd LPSC*, Abs. 2097. Presented at the Lunar and Planetary Science Conference.
- Lauretta, D. S., Enos, H. L., Polit, A. T., Roper, H. L., Wolner, C. W. V. (2021). OSIRIS-REx at Benu: Overcoming challenges to collect a sample of the early solar system, in *Sample Return Missions*, ed. Longobardo, A. (Elsevier, in press), ch. 8, doi:10.1016/C2018-0-03374-5.
- Lee, J.-C., Massironi, M., Ip, W.-H., Giacomini, L., Ferrari, S., Penasa, L., et al. (2016). Geomorphological mapping of comet 67P/Churyumov–Gerasimenko’s Southern hemisphere. *Monthly Notices of the Royal Astronomical Society*, 462(Suppl_1), S573–S592. <https://doi.org/10.1093/mnras/stx450>
- Leonard, J. M., Adam, C. D., Pelgrift, J. Y., Lessac-Chenen, E. J., Nelson, D. S., Antreasian, P. G., et al. (2020). Initial Orbit Determination and Event Reconstruction From Estimation of Particle Trajectories About (101955) Benu. *Earth and Space Science*, 7(9), e2019EA000937. <https://doi.org/10.1029/2019EA000937>

- Michel, P., Ballouz, R.-L., Barnouin, O. S., Jutzi, M., Walsh, K. J., May, B. H., et al. (2020). Collisional formation of top-shaped asteroids and implications for the origins of Ryugu and Bennu. *Nature Communications*, 11(1), 2655. <https://doi.org/10.1038/s41467-020-16433-z>
- Michel, P., Kueppers, M., Sierks, H., Carnelli, I., Cheng, A. F., Mellab, K., et al. (2018). European component of the AIDA mission to a binary asteroid: Characterization and interpretation of the impact of the DART mission. *Advances in Space Research*, 62(8), 2261–2272. <https://doi.org/10.1016/j.asr.2017.12.020>
- Molaro, J. L., Walsh, K. J., Jawin, E. R., Ballouz, R.-L., Bennett, C. A., DellaGiustina, D. N., et al. (2020). In situ evidence of thermally induced rock breakdown widespread on Bennu's surface. *Nature Communications*, 11(1), 2913. <https://doi.org/10.1038/s41467-020-16528-7>
- Miyamoto, H., Hemmi, R., Kikuchi, H., Komatsu, G., Honda, C., Michikami, T., et al. (2019). Geomorphological Characteristics of Asteroid Ryugu and its Preliminary Geologic Map, 50th LPSC, Abs. 2398. Presented at the Lunar and Planetary Science Conference.
- Nolan, M. C., Magri, C., Howell, E. S., Benner, L. A. M., Giorgini, J. D., Hergenrother, C. W., et al. (2013). Shape model and surface properties of the OSIRIS-REx target Asteroid (101955) Bennu from radar and lightcurve observations. *Icarus*, 226(1), 629–640. <https://doi.org/10.1016/j.icarus.2013.05.028>
- Pelgrift, J. Y., Lessac-Chenen, E. J., Adam, C. D., Leonard, J. M., Nelson, D. S., McCarthy, L., et al. (2020). Reconstruction of Bennu Particle Events From Sparse Data. *Earth and Space Science*, 7(8), e2019EA000938. <https://doi.org/10.1029/2019EA000938>
- Perry, M. E., Barnouin, O. S., Jawin, E. R., Walsh, K. J., Pajola, M., Daly, M. G., et al. (2019). Topographic Lineaments on Bennu, 50th LPSC, Abs. 2951. Presented at the Lunar and Planetary Science Conference.
- Perry et al., Impact-crater ejecta on Bennu indicate a surface with very low strength, in review at *Nature Geoscience*
- Reuter, D. C., A. A. Simon, J. Hair, A. Lunsford, S. Manthripragada, V. Bly, B. Bos, C. Brambora, E. Caldwell, C. Casto, Z. Dolch, P. Finneran, D. Jennings, M. Jhabvala, E. Matson, M. McLelland, W. Roher, T. Sullivan, E. Weigle, Y. Wen, D. Wilson, D. S. Lauretta (2018). The OSIRIS-REx Visible and Infrared Spectrometer (OVIRS): Spectral maps of the asteroid Bennu. *Space Sci. Rev.*, 214, 54.
- Rizos, J. L., de León, J., Licandro, J., Golish, D. R., Campins, H., Tatsumi, E., et al. (2021). Bennu's global surface and two candidate sample sites characterized by spectral clustering of OSIRIS-REx multispectral images. *Icarus*, 114467. <https://doi.org/10.1016/j.icarus.2021.114467>
- Rizk, B. et al. (2018). OCAMS: The OSIRIS-REx Camera Suite. *Space Sci. Rev.* 214, 26. <https://doi.org/10.1007/s11214-017-0460-7>
- Roberts et al., (2021). Rotational states and shapes of Ryugu and Bennu Implications for interior structure and strength. *Planetary & Space Science*, 204, 105268, <https://doi.org/10.1016/j.pss.2021.105268>
- Rozitis, B., Ryan, A. J., Emery, J. P., Christensen, P. R., Hamilton, V. E., Simon, A. A., et al. (2020). Asteroid (101955) Bennu's weak boulders and thermally anomalous equator. *Science Advances*, 6(41), eabc3699. <https://doi.org/10.1126/sciadv.abc3699>
- Seabrook, J.A. et al. (2019). Global shape modeling using the OSIRIS-REx scanning laser altimeter. *Planet. Space Sci.* 177, 104688. <https://doi.org/10.1016/j.pss.2019.07.003>

- Scheeres, D. J., McMahon, J. W., French, A. S., Brack, D. N., Chesley, S. R., Farnocchia, D., et al. (2019). The dynamic geophysical environment of (101955) Benu based on OSIRIS-REx measurements. *Nature Astronomy*. <https://doi.org/10.1038/s41550-019-0721-3>
- Scheeres, D. J., French, A. S., Tricarico, P., Chesley, S. R., Takahashi, Y., Farnocchia, D., et al. (2020). Heterogeneous mass distribution of the rubble-pile asteroid (101955) Benu. *Science Advances*, 6(41), eabc3350. <https://doi.org/10.1126/sciadv.abc3350>
- Simon, A. A., Kaplan, H. H., Hamilton, V. E., Lauretta, D. S., Campins, H., Emery, J. P., et al. (2020). Widespread carbon-bearing materials on near-Earth asteroid (101955) Benu. *Science*. <https://doi.org/10.1126/science.abc3522>
- Sugita, S., Honda, R., Morota, T., Kameda, S., Sawada, H., Tatsumi, E., et al. (2019). The geomorphology, color, and thermal properties of Ryugu: Implications for parent-body processes. *Science*, 364(6437). <https://doi.org/10.1126/science.aaw0422>
- Tatsumi, E. and Sugita, S. (2018). Cratering efficiency on coarse-grained targets: Implications for the dynamical evolution of asteroid 25143 Itokawa. *Icarus*, 300, 227-248. <https://doi.org/10.1016/j.icarus.2017.09.004>
- Walsh, K. J., Richardson, D. C., & Michel, P. (2008). Rotational breakup as the origin of small binary asteroids. *Nature*, 454(7201), 188–191. <https://doi.org/10.1038/nature07078>
- Walsh, K. J., Jawin, E. R., Ballouz, R.-L., Barnouin, O. S., Bierhaus, E. B., Connolly, H. C., et al. (2019). Craters, boulders and regolith of (101955) Benu indicative of an old and dynamic surface. *Nature Geoscience*, 12(4), 242–246. <https://doi.org/10.1038/s41561-019-0326-6>
- Watanabe, S., Hirabayashi, M., Hirata, N., Hirata, N., Noguchi, R., Shimaki, Y., et al. (2019). Hayabusa2 arrives at the carbonaceous asteroid 162173 Ryugu—A spinning top-shaped rubble pile. *Science*, 364(6437), 268–272. <https://doi.org/10.1126/science.aav8032>
- Zhang et al. (2020) Numerical modeling of Benu's structural stability and implications for its internal and surface properties, EPSC2020-722, Vol. 14, <https://doi.org/10.5194/epsc2020-722>

Figures and Tables

Figures associated with the manuscript: 18 figures

Tables: 7 tables

Figure 1. Global mosaics and shape model used in this work. (A) Detailed Survey mosaic with pixel scale ~ 5 cm (Bennett et al., 2021). This higher-resolution mosaic covers the poles and is useful for identifying small-scale features and boundaries, but contains an image seam around the equatorial region. Therefore both mosaics were used for mapping. (B) Approach mosaic with pixel scale of ~ 40 cm (DellaGiustina et al., 2019). This mosaic is well suited to assessing surface texture and subtle shape features, but does not contain polar coverage. (C) OLA 20-cm-resolution shape model (Barnouin et al., 2020) with shaded facet radius, used for mapping shape features and for 3D mapping in SBMT.

Figure 2. OLA surface roughness proxy map (M.G. Daly et al., 2020) shown in (A) equirectangular and (B) polar projections. Roughness is expressed in terms of the standard deviation of OLA returns within a moving 30-cm window, where larger values correspond to rougher regions.

Figure 3. Bennu's shape features. Outline of the equatorial bulge (defined by 250-m radius contour) shown in thick solid lines. Approximate locations of four longitudinal ridges (LR) shown in thin dashed lines, from M.G. Daly et al. (2020). Basemap is the Detailed Survey mosaic with shaded facet radius overlay in (A) equatorial and (B) polar projection.

Figure 4. Distribution of high-standing regions on Bennu in (A) equirectangular and (B) polar projections. **Supplementary Figure 1** shows these features mapped in 3D in SBMT. The approximate locations of longitudinal ridges in dashed white lines is similar to the mapped high-standing regions, although the number and extent is different; one high-standing region spans the northern hemisphere, crossing the pole, while a second is in the southern hemisphere, reaching the pole. A third high-standing region is isolated to the equatorial region and part of the mid-latitudes. Basemap is the Detailed Survey mosaic with shaded facet radius overlay. Low-lying regions are mapped as the region not covered by high-standing regions (**Supplementary Figure 2**). High-standing regions cover $\sim 46\%$ of Bennu's surface, while low-lying regions cover 54%.

Figure 5. Craters and lineaments. Global map in equirectangular projection with the Detailed Survey mosaic. Note that the projection distorts high-latitude regions, so craters near the poles and the E-W lineament will appear artificially wide. Numbers indicate lineament labels in **Table 1**. White arrow indicates the lineament in **Figure 6**.

Figure 6. The most distinct scarp-like lineament on Bennu, centered $\sim 220^\circ\text{E}$, 20°S (lineament 3, **Table 1**). Location indicated by arrows, and white arrow in **Figure 5**. This N-S curvilinear scarp contains the largest elevation difference of the mapped lineaments, with ~ 10 m relief. The low-elevation region to the east of the scarp contains an accumulation of boulders, potentially indicating a slope collapse and subsequent landslide. This region has the highest concentrations of boulders on Bennu (Walsh et al., 2019).

Figure 7. Saxa (boulders), mass movement, PE source regions. (A) Global distribution of features shown on Detailed Survey mosaic. Two PE source regions connected by the white dashed line are the near and far radiant points for the 6 January event. (B) Saxum associated with mass movement, suggesting the boulder has been partly buried, as discussed in Jawin et al. (2020a). (C) Smooth lobate deposit (magenta arrows) located inside Minokawa Crater (eastern crater rim indicated with white arrows), portion of MapCam image ocams20181213t050008s628. Extent of (B) and (C) are shown in white boxes in (A).

Figure 8. Map of geologic features on Bennu with mapped features from **Figures 5 and 7**, and the location of the OSIRIS-REx Nightingale sample site.

Figure 9. Map of distinct surface textures on Bennu. (A) Basemap is the Approach mosaic as this best highlights surface texture variations showing smooth/knobby regions (yellow outlines) and rugged regions (red outlines). Many regions on Bennu's surface are not distinctly smooth/knobby or rugged, but appear to belong to an intermediate physiographic group (corresponding to unmapped regions in the map). (B-C) Typical surface textures in the smooth/knobby regions and rugged regions. Extents outlined in black boxes in (A).

Figure 10. Two geologic units on Bennu. (A) Unit boundaries defined by surface morphology, geologic feature distribution, and shape features, on the Approach mosaic. (B) The unit boundaries define two units: Smooth Unit (orange shaded region), and Rugged Unit (shaded blue region), on the Approach mosaic. (C-D) Same geologic units shown on the Detailed Survey mosaic in equirectangular and polar projections.

Figure 11. Geologic units on morphologic map. There is good agreement between the smooth/knobby and rugged surface texture regions (yellow and red outlines, respectively) and the Smooth and Rugged geologic units (orange shaded regions and blue shaded regions, respectively). Not all regions on Bennu were included in the surface texture map, so the geologic units are larger and more inclusive than the surface texture regions. The only discrepancy in the surface texture map and the geologic unit map is the smooth/knobby region at $\sim 270^\circ\text{E}$, 5°S which was mapped as the smooth lobate deposit in the geologic feature map (**Figure 7**). As this feature is <100 m across, it was not sufficiently large to be mapped as a separate portion of the Smooth Unit.

Figure 12. Global geologic map, including the two geologic units and all geologic features in (A) equirectangular and (B) polar projections. Most saxa and mass movement features are located in the Rugged Unit. Lineaments serve as unit boundaries in several locations. The smooth unit contains more craters per unit area by a factor of ~ 2 than the Smooth Unit.

Figure 13. Geologic units on shape feature map in (A) equirectangular and (B) polar projection. Shape features include the equatorial bulge (thick white lines) and the high-standing regions (indicated by hatched regions). Note that low-lying regions are mapped as all regions not covered by high-standing regions. The two geologic units are not strongly affected by the boundary or the extent of the equatorial bulge. The geologic units also do not have a strong correlation with the mapped high-standing and low-lying regions, although the N-S orientation of the units is similar to that of the high-standing and low-lying regions, suggesting the shape may have played a relatively minor role in the formation and evolution of the geologic units.

Figure 14. Comparisons of geologic unit boundaries to the OLA surface roughness proxy map. (A) Unit boundaries (white outline) distinguish between rougher and smoother regions on the surface. (B) Surface roughness proxy binned into values greater and less than the global median roughness (0.11 m). The Rugged Unit contains all of the spatially extensive regions with roughness values greater than the global median. The poles are smoother than the median, and are entirely within the Smooth Unit.

Figure 15. Geologic units shown on other global data sets. (A) Map of PolyCam normal albedo with colored contours at intervals of 0.0005 (cool colors: lower albedo, warm colors: higher albedo). Unit boundaries (white lines) demarcate the Smooth and Rugged Unit. The smooth unit generally corresponds to regions of higher albedo, while the rugged unit covers most of the lowest-albedo regions, which often correspond to the locations of large boulders. Map adapted from Golish et al. (2021). (B)OTES spectral Type 1/Type 2 ratio. Type 2 spectra are consistent with thin dust coatings over larger particles, and are spatially correlated with the locations of large boulders. Map adapted from Hammon et al. (2021).

Figure 16. Global crater differential SFD. Number of craters per diameter bin, divided by crater diameter, and scaled by surface area of Bennu (0.787 km^2 for the full distribution, green curve; 0.35 km^2 for the Smooth Unit, orange curve; 0.44 km^2 for the Rugged Unit, blue curve). Note the “fish hook” shape of the distribution at craters ~ 2.3 m diameter in the global distribution (green curve) (Bierhaus et al., 2022), which persists across both geologic units (orange and blue curves). The Rugged Unit contains a depletion of craters < 20 m diameter relative to the Smooth Unit, suggesting craters have been removed due to resurfacing. The Smooth Unit is older than the Rugged Unit.

Figure 17. Distribution of the reddest (youngest) craters on Bennu, from DellaGiustina et al. (2020). The Rugged Unit contains a factor of ~ 3 fewer red craters than the Smooth Unit (scaled for surface area), implying it has been resurfaced on a similar timescales to that in which the craters formed, ~ 100 -500 kyr.

Figure 18. Timeline summarizing the major geologic events and approximate ages on Bennu.

Table 1. Lineament location and morphologic type

Lineament	Endpoint 1	Endpoint 2	Length (m)
1	117°E, 21°S	113°E, 44°S	101
2	155°E, 23°S	153°E, 51°S	115
3	220°E, 2°N	242°E, 36°S	195
4	201°E, 36°N	214°E, 9°N	132
5	202°E, 53°N	255°E, 57°N	118

Table 2. Particle Ejection events and source regions

PE Event ^a		Longitude	Latitude
6 Jan 2019	Near	325.3 ^{+18.9} -10.3	-75.0 ^{+12.7} -2.8
	Far	343.7 ^{+3.8} -14.7	-57.3 ^{+1.5} -17.5
19 Jan 2019		335.4 ± 0.4	19.9 ± 0.9
11 Feb 2019		59.7 ± 0.3	15.1 ± 0.7
19 Apr 2019		225.2 ± 2.5	18.6 ± 1.0
13 Sep 2019		20.6 ± 1.5	-65.4 ± 0.3

^a Ejection dates and locations as reported by Hergenrother et al., 2020.

Table 3. Distribution of geologic features in the geologic units

Geologic Feature	Smooth Unit (N)	Smooth Unit (%) ^a	Rugged Unit (N)	Rugged Unit (%) ^a
Saxa	4	11%	32	89%
Mass movement	13	15%	74	85%
Craters (>20 m) ^b	43	57%	33	43%
Craters (10–20 m)	47	63%	28	37%

^a Percent values have not been scaled for surface area (Smooth Unit is 44%, Rugged Unit is 56% of Bennu's total surface area)

^b Large craters that span both units and are approximately equally distributed were not included

Table 4. Percent of each shape feature covered by the geologic units

Shape Feature	Smooth Unit	Rugged Unit
Equatorial bulge	57%	43%
High-standing regions	68%	32%
Low-lying regions	46%	54%

Table 5. Slopes in each geologic unit at different shape model resolutions

Unit		Very Low	Medium	Very High
	Facet size	~6 m	~3 m	~1 m
Rugged	Median	16°	20°	29°
	Std (1 σ)	9°	15°	20°
Smooth	Median	15°	17°	21°
	Std (1 σ)	7°	11°	16°

Table 6. Distribution of the reddest craters across geologic units

Craters		Smooth Unit (N)	Smooth Unit (%)	Rugged Unit (N)	Rugged Unit (%)
1 σ	79	53	67	26	33
0.5 σ	255	182	71	73	29

Table 7. Description of Map Units

Property or Feature	Smooth Unit	Rugged Unit
Surface area (total: 0.787 km ²)	0.346 km ² (44%)	0.441 km ² (56%)
Surface texture	Smooth/knobby, few boulders	Rugged, abundant boulders
Boulder abundance (>20 m) ^a	12 per km ²	73 per km ²
Crater abundance (>10 m) ^a	260 per km ²	138 per km ²
Mass movement feature abundance ^a	35 per km ²	168 per km ²
Range of slopes ^b	0.060 – 91° (median: 17°)	0.020 – 99° (median: 20°)
Range of surface roughness	0 – 4.6 m (median: 0.33 m)	0 – 8.6 m (median: 0.36 m)
Albedo range ^c	0.019 – 0.30 (median: 0.048)	0.018 – 0.30 (median: 0.046)
Thermal emission spectral characteristics	Abundant OTES spectral Type 1 material	Abundant OTES spectral Type 2 material
Thermal inertia range ^{c, d}	45 – 423 J m ⁻² K ⁻¹ s ^{-1/2} (median: 314 J m ⁻² K ⁻¹ s ^{-1/2})	143 – 459 J m ⁻² K ⁻¹ s ^{-1/2} (median: 318 J m ⁻² K ⁻¹ s ^{-1/2})
Thermal roughness range ^c	20 – 54° (median: 38°)	8.7 – 54° (median: 41°)

^a Number of geologic features scaled for surface area of each geologic unit (see Table 3)

^b Taken from the medium resolution shape model (see Table 5)

^c Dataset does not have global coverage, lacks data over the poles

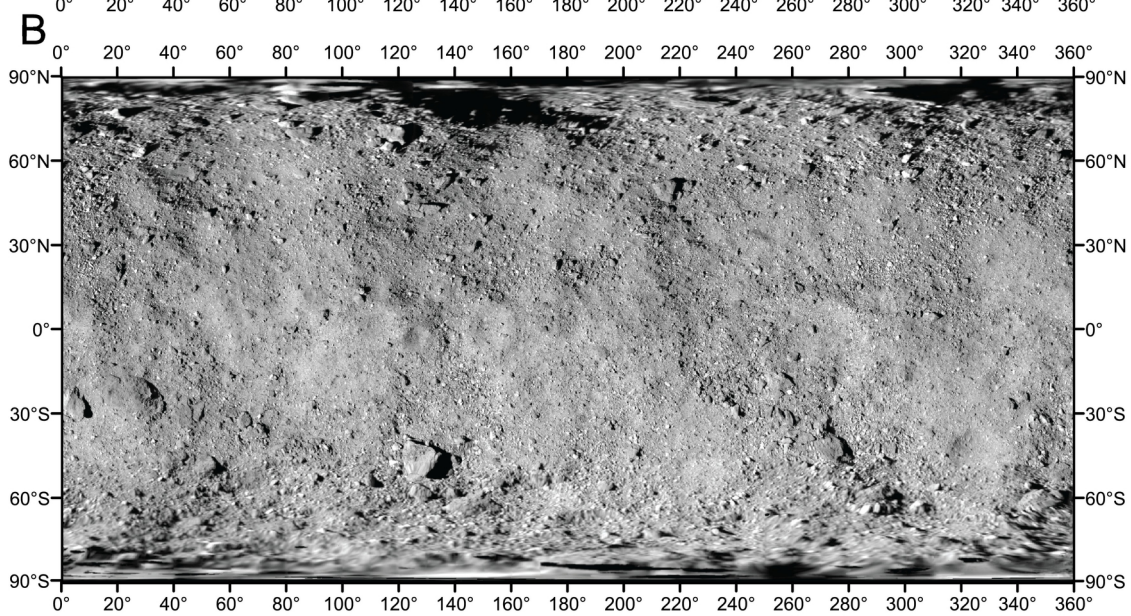
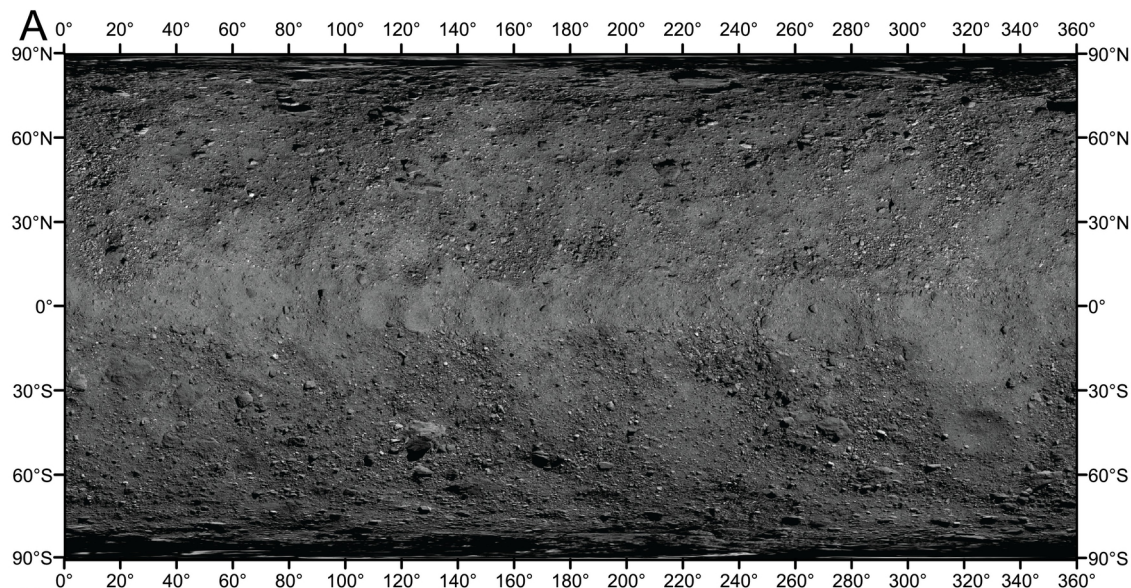
^d Thermal inertia spatial variation does not closely match the geologic unit boundaries

Journal Pre-proof

Highlights:

- We created a global geologic map of rubble-pile asteroid Bennu
- Two geologic units are present: one smooth, one rugged
- The Smooth Unit is a >2 Myr old surface that was shaped in the Main Asteroid Belt
- The Rugged Unit was resurfaced via mass movement in the past ~ 0.5 Myr

Journal Pre-proof



C

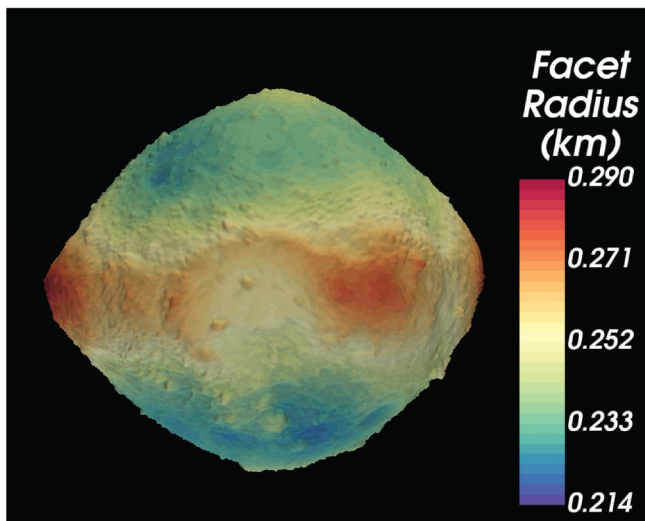


Figure 1

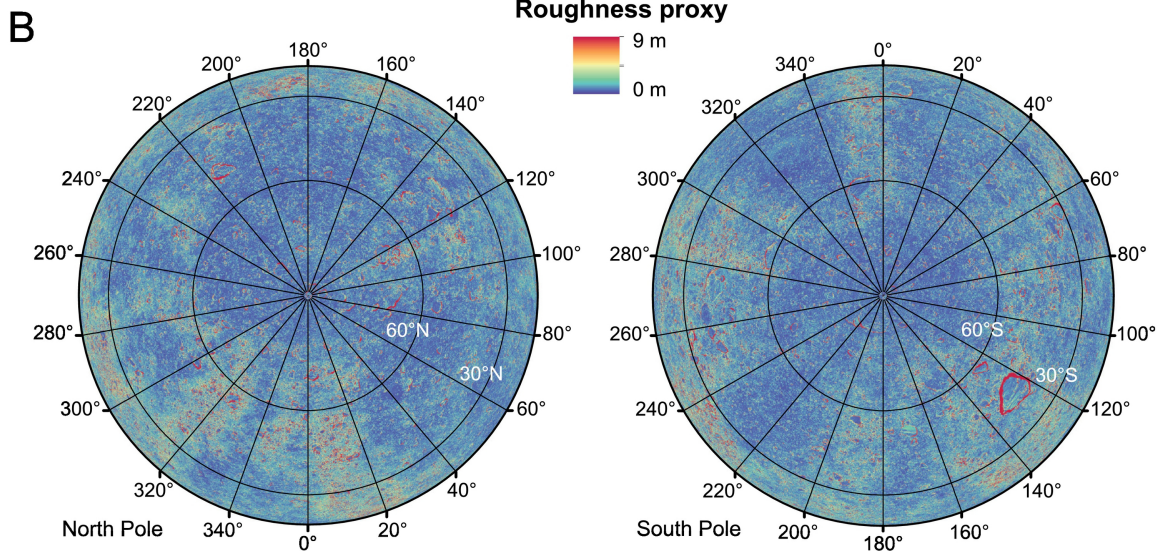
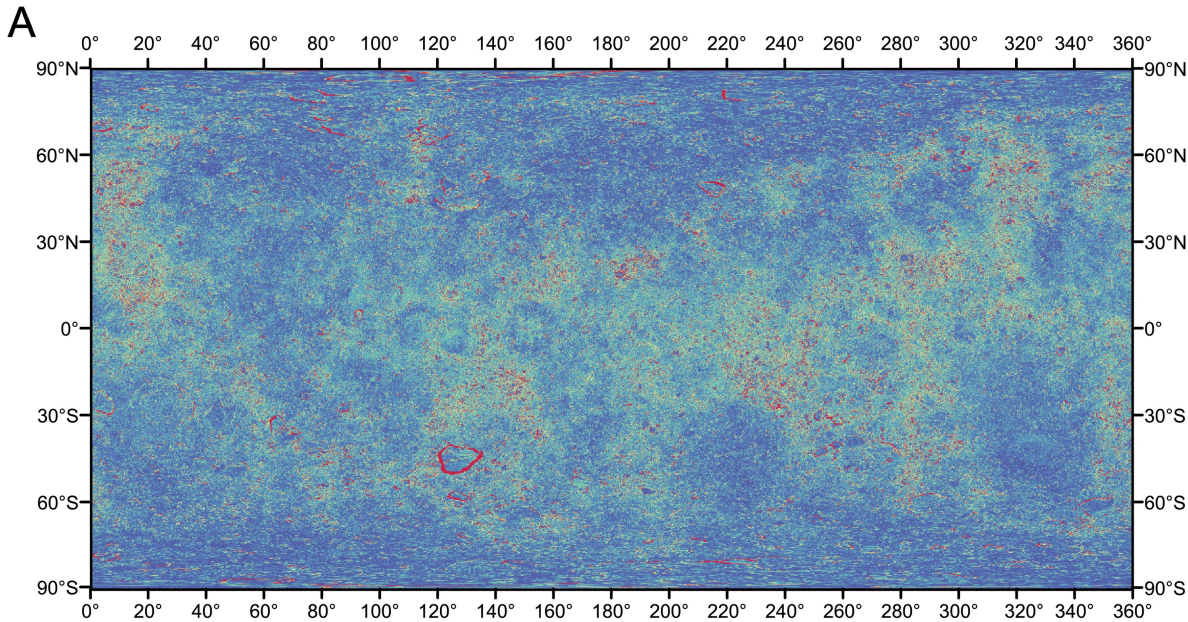
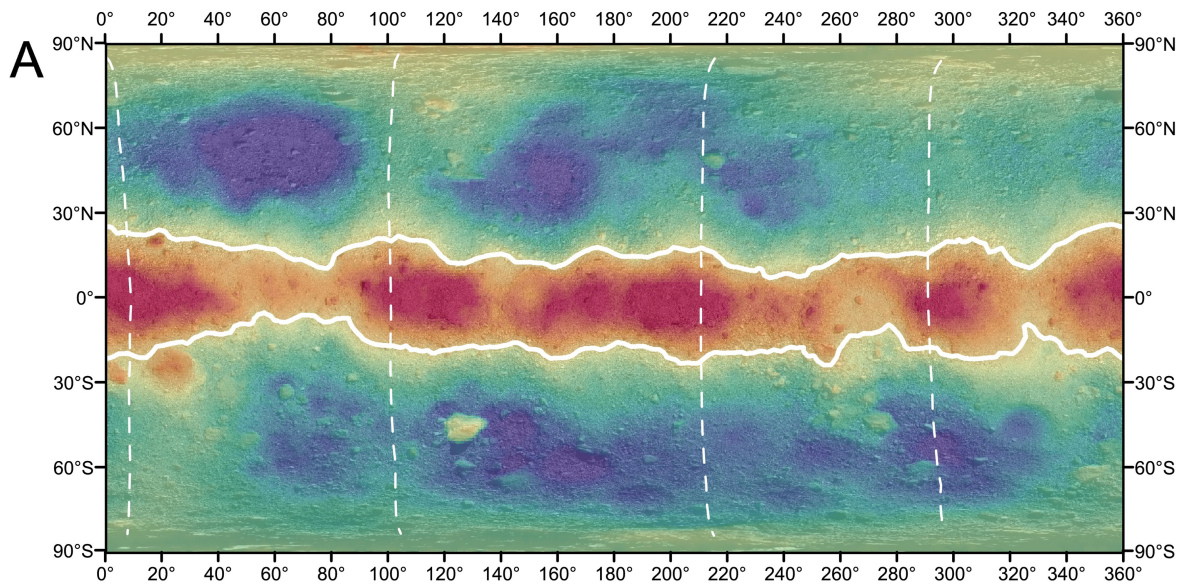


Figure 2



Facet Radius — Equatorial Bulge --- Approx LR

290 m

214 m

B

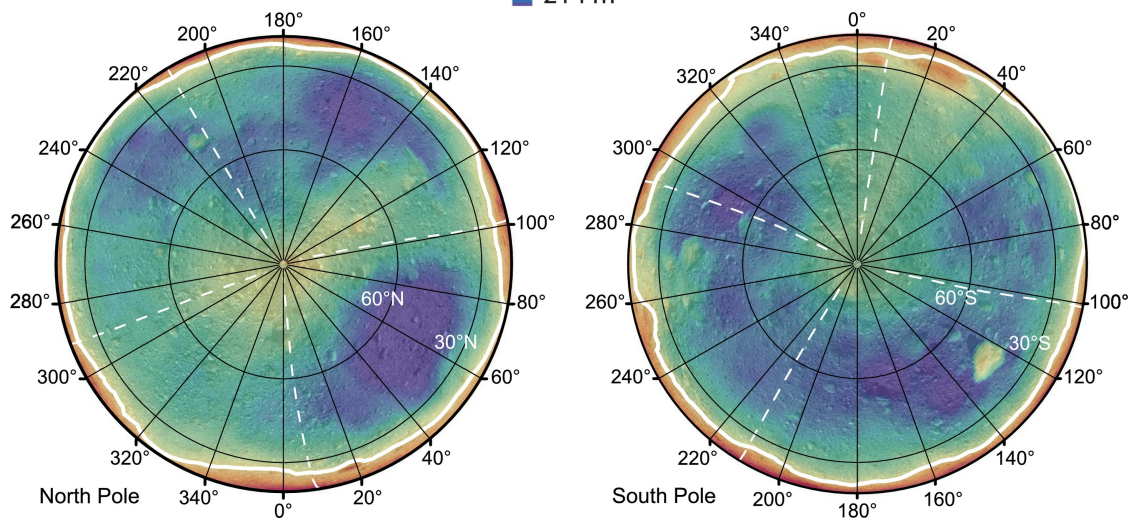


Figure 3

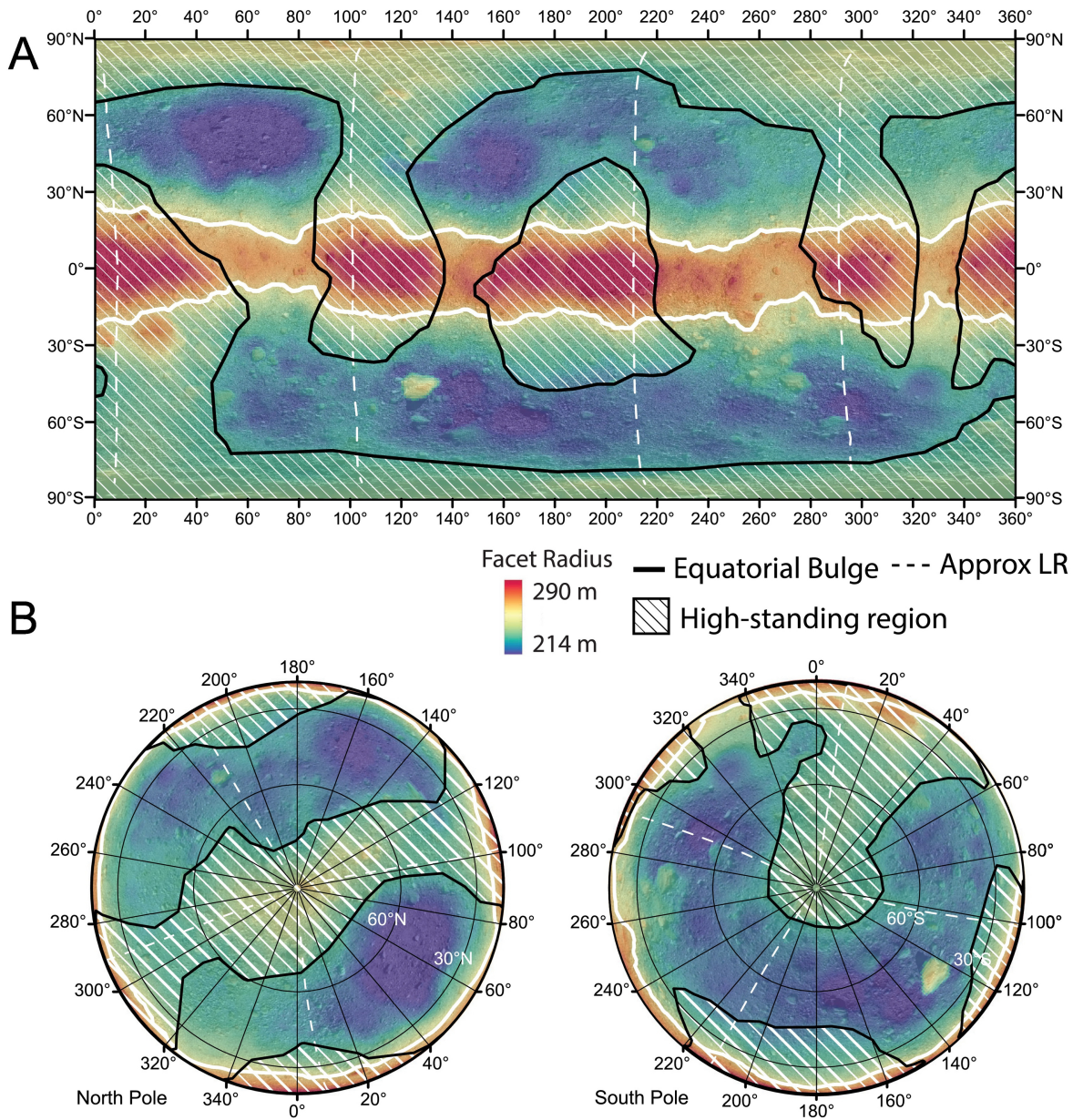


Figure 4

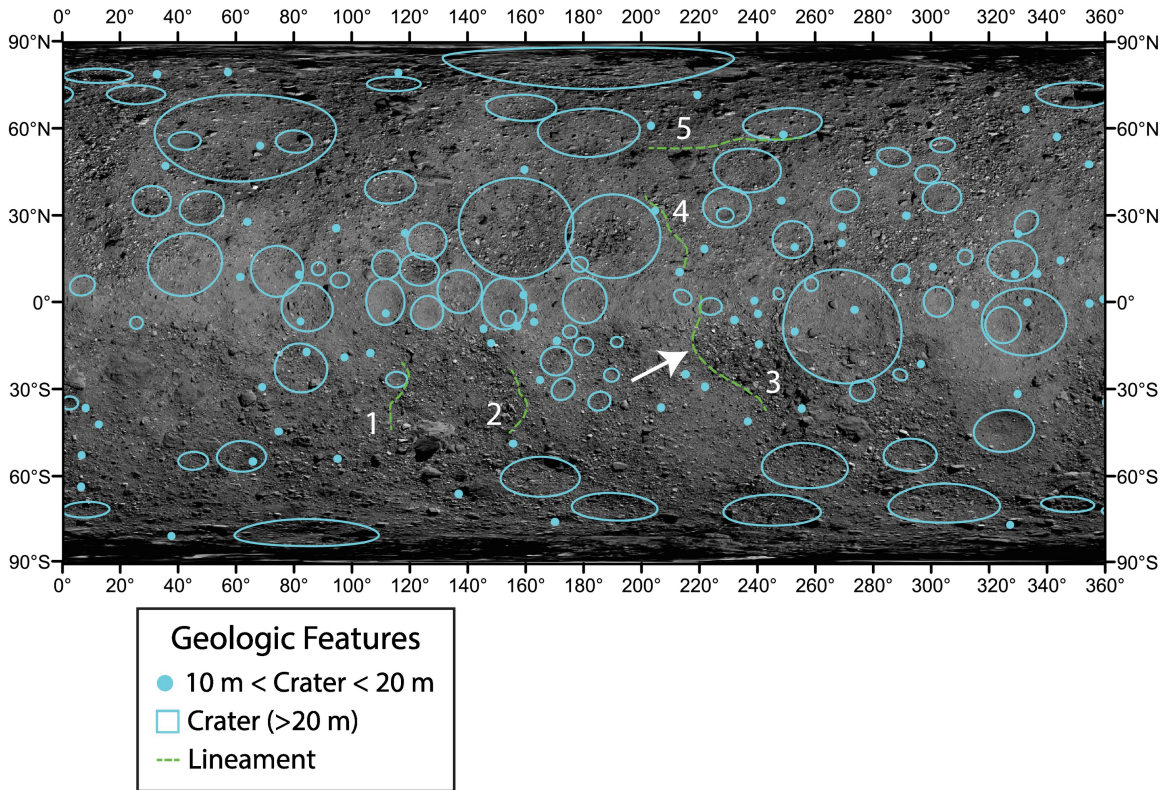
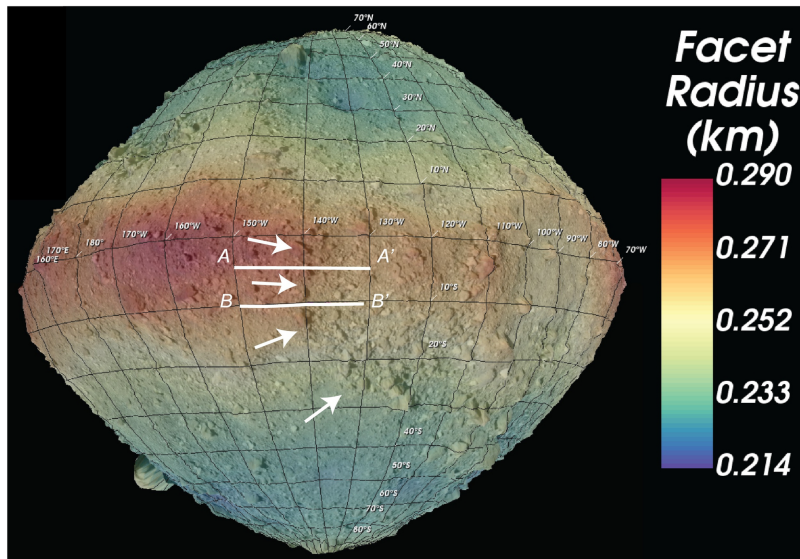


Figure 5

A



B

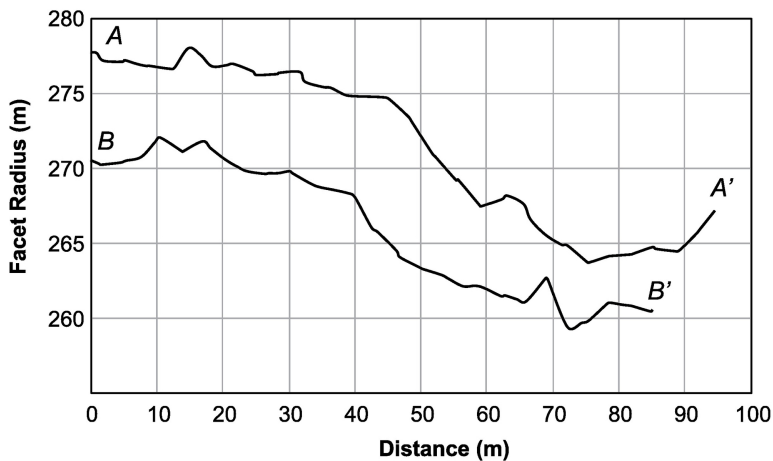


Figure 6

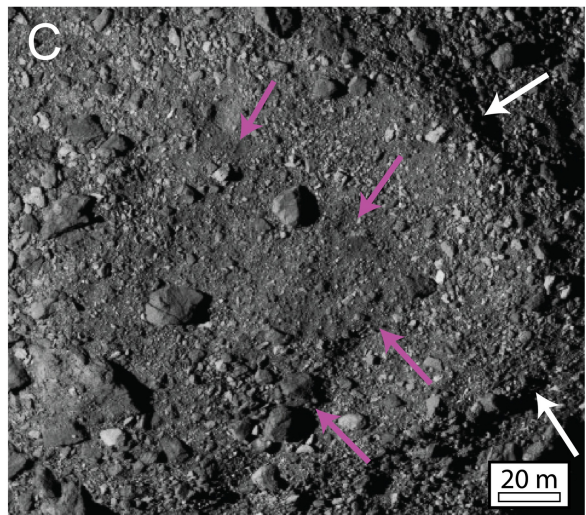
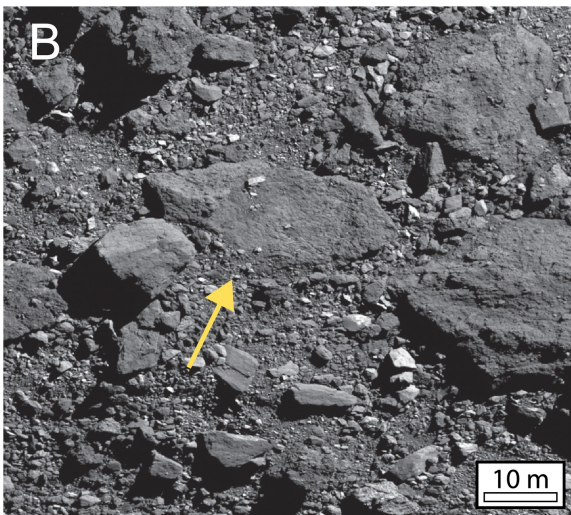
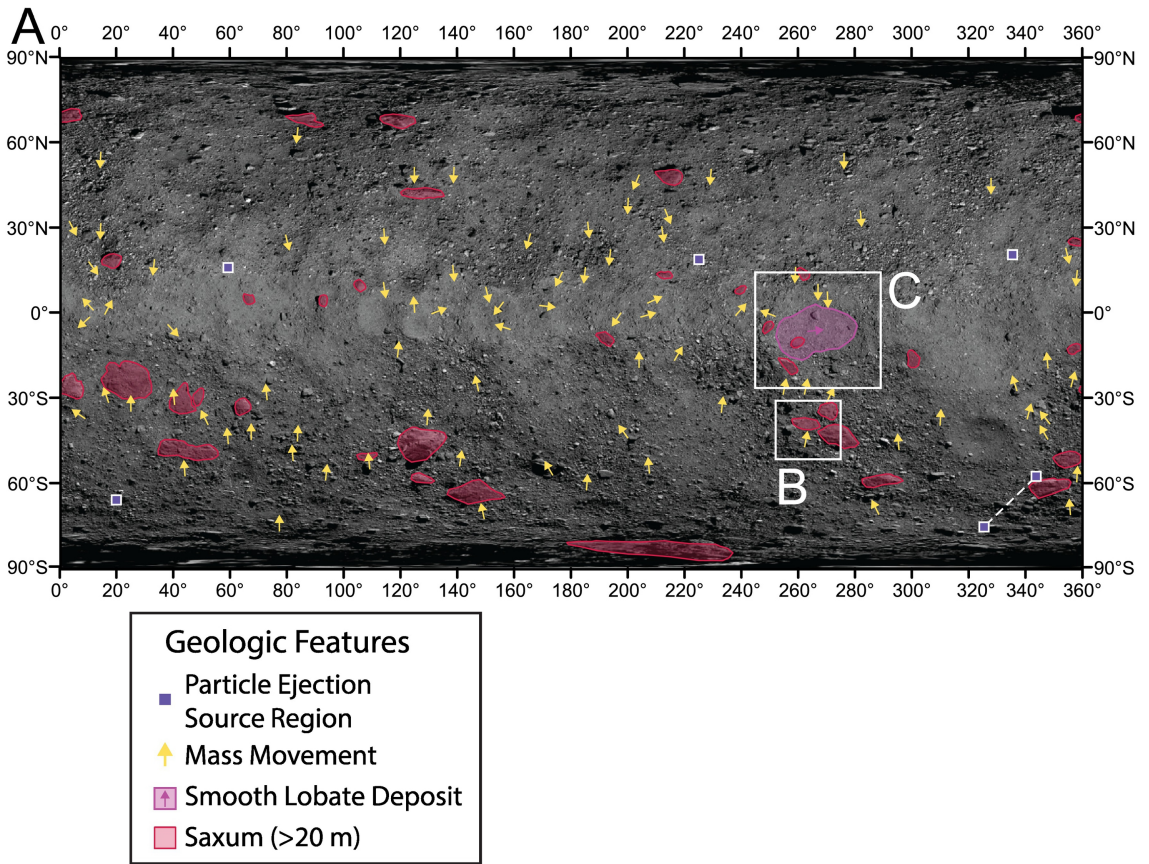


Figure 7

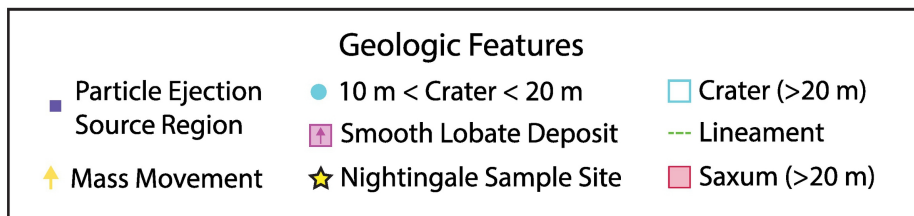
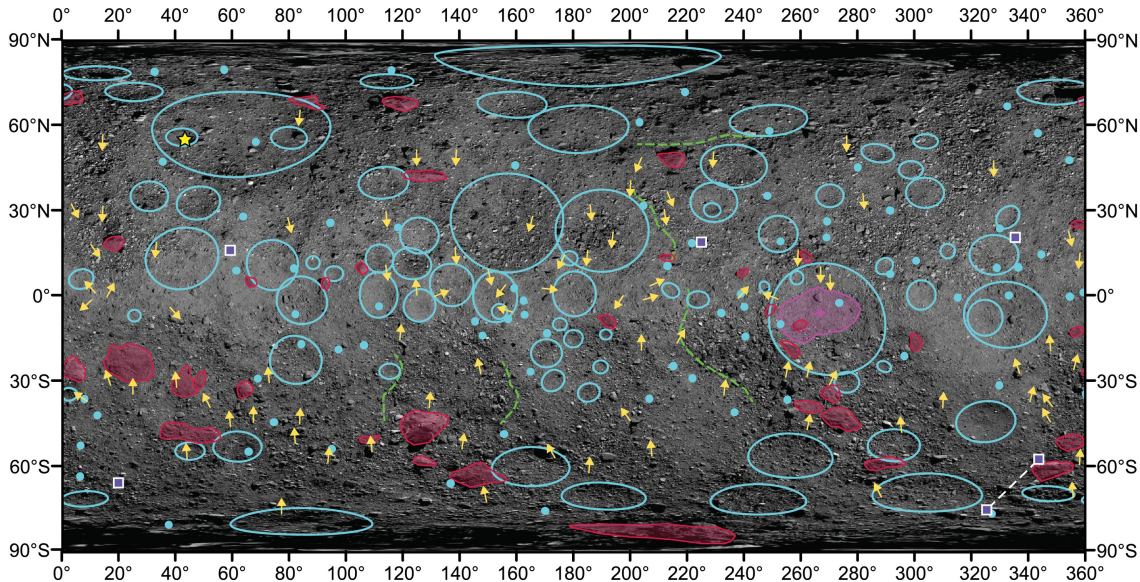


Figure 8

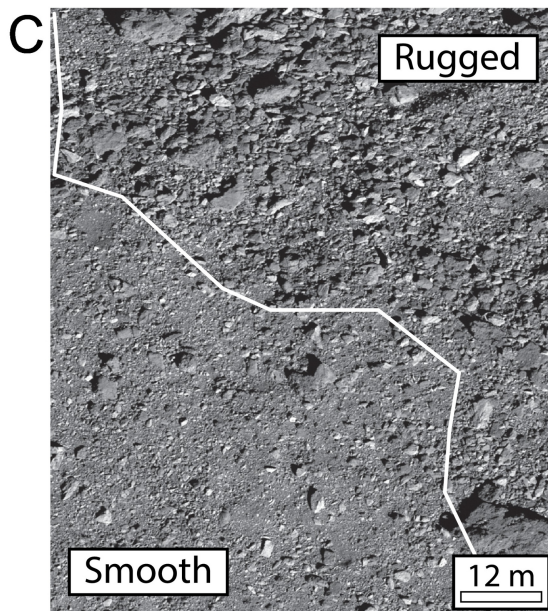
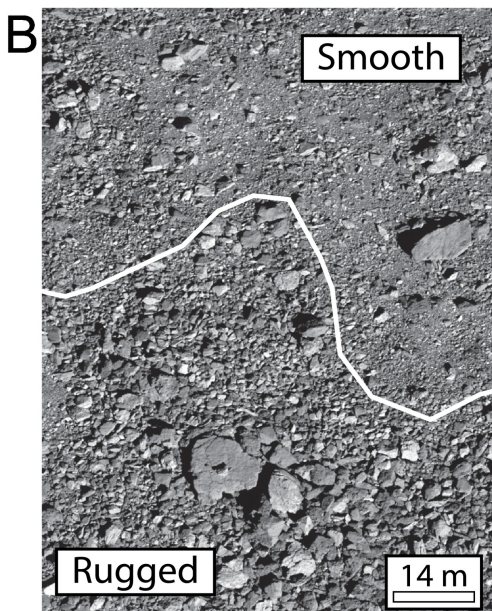
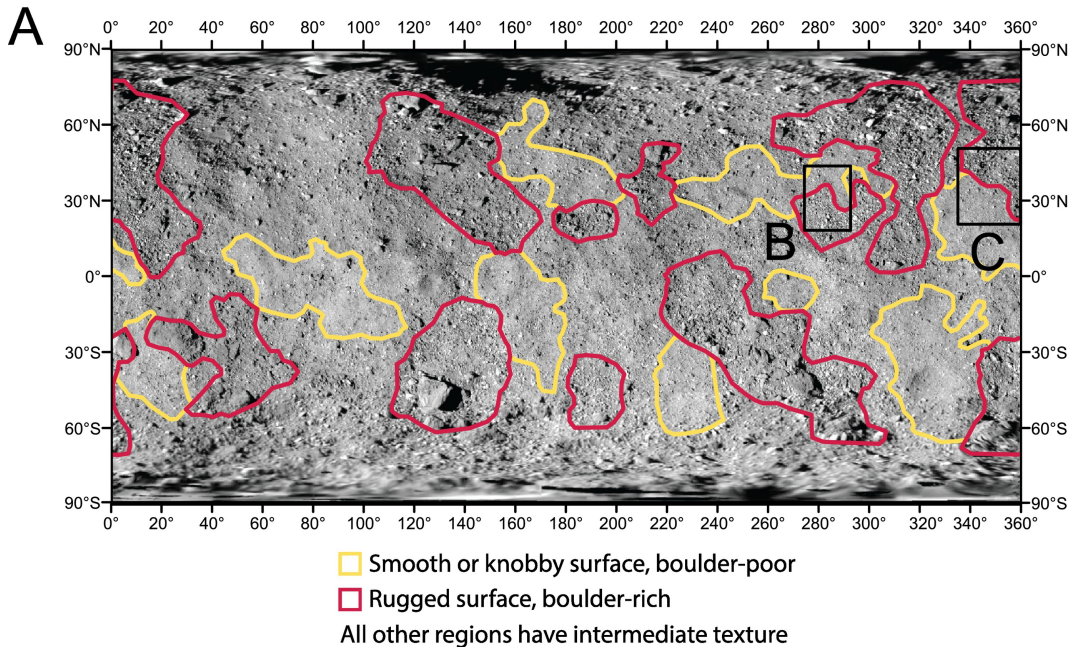
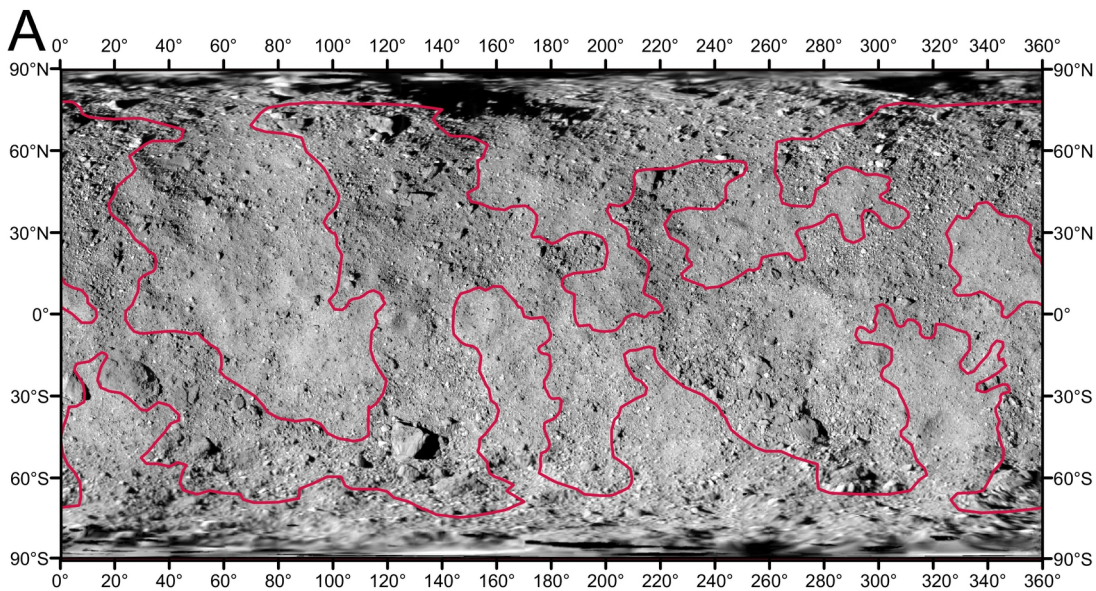


Figure 9



□ Unit boundaries

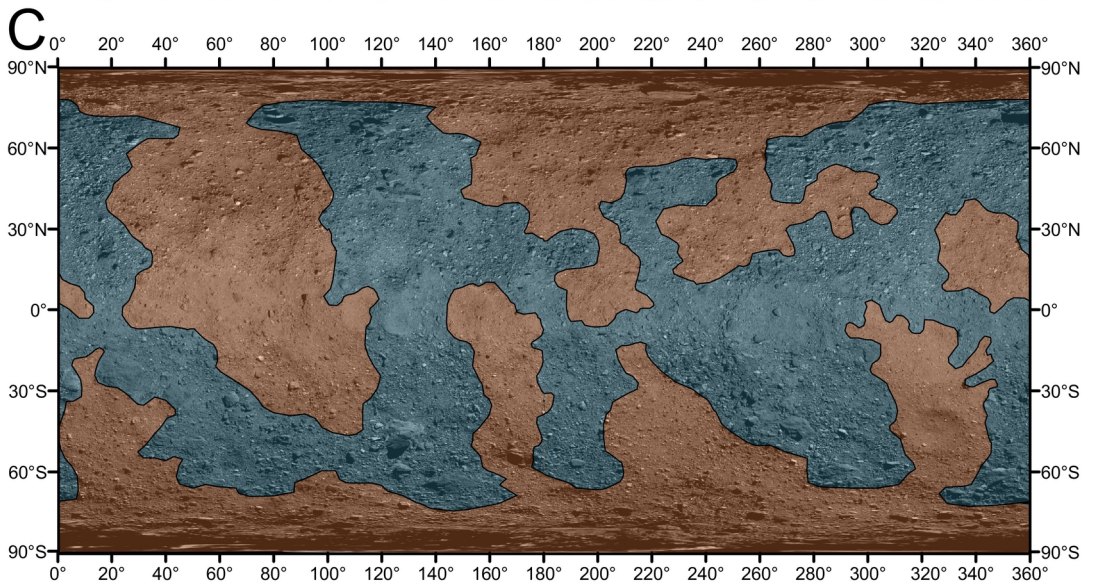
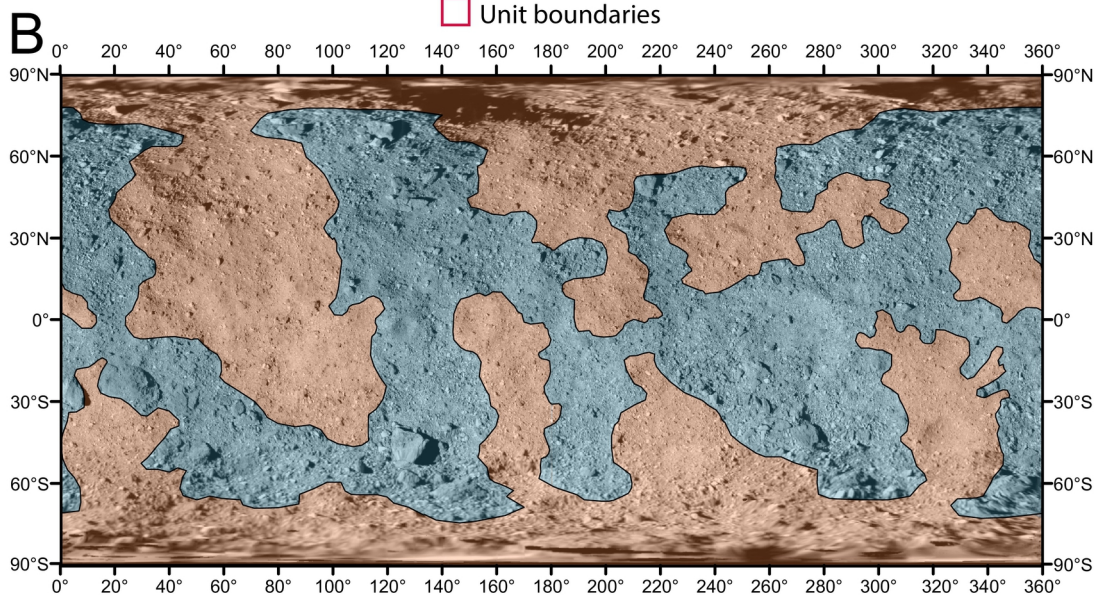
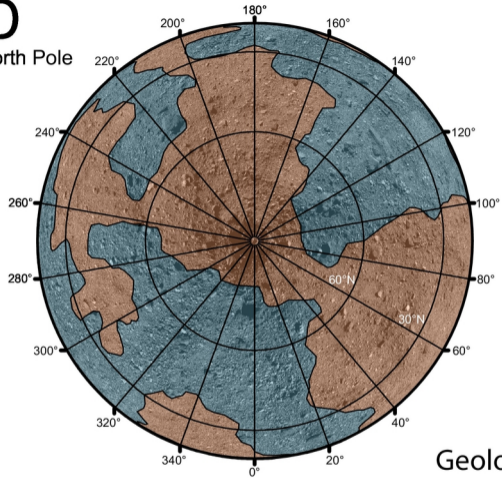


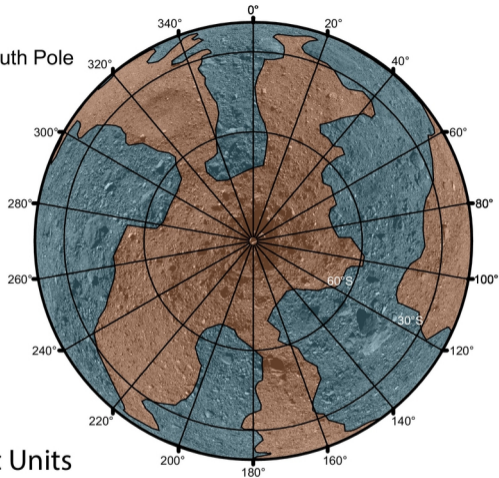
Figure 10A

D

North Pole



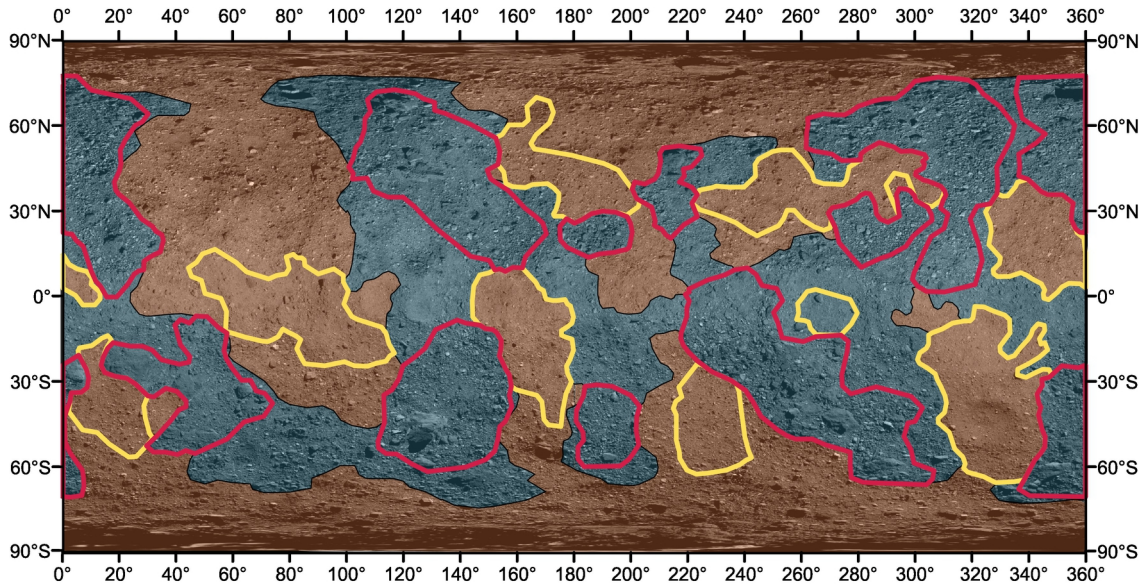
South Pole



Geologic Units

Smooth Unit Rugged Unit

Figure 10B







- | | |
|--|--|
|  Smooth or knobby surface, boulder-poor |  Smooth Unit |
|  Rugged surface, boulder-rich |  Rugged Unit |

Figure 11

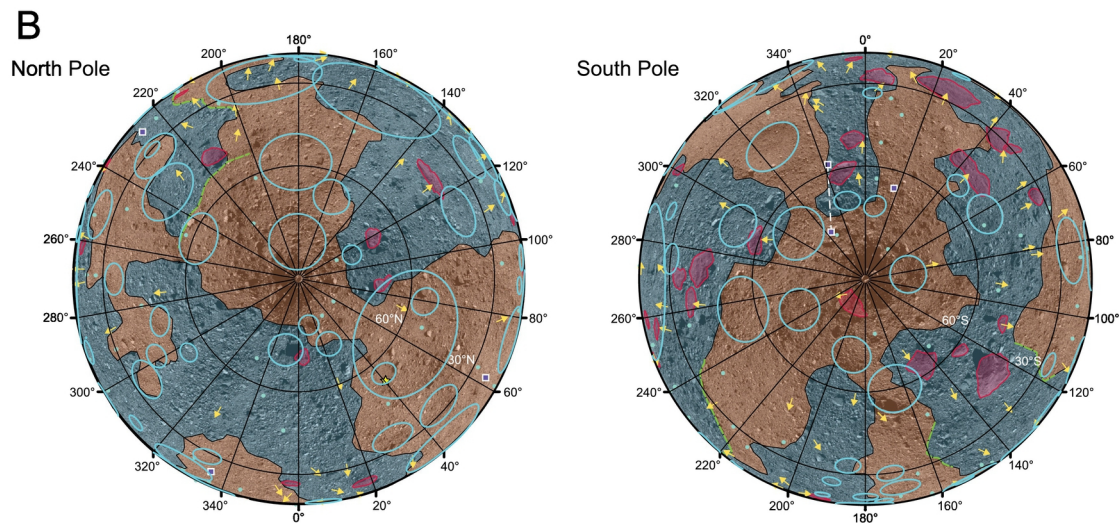
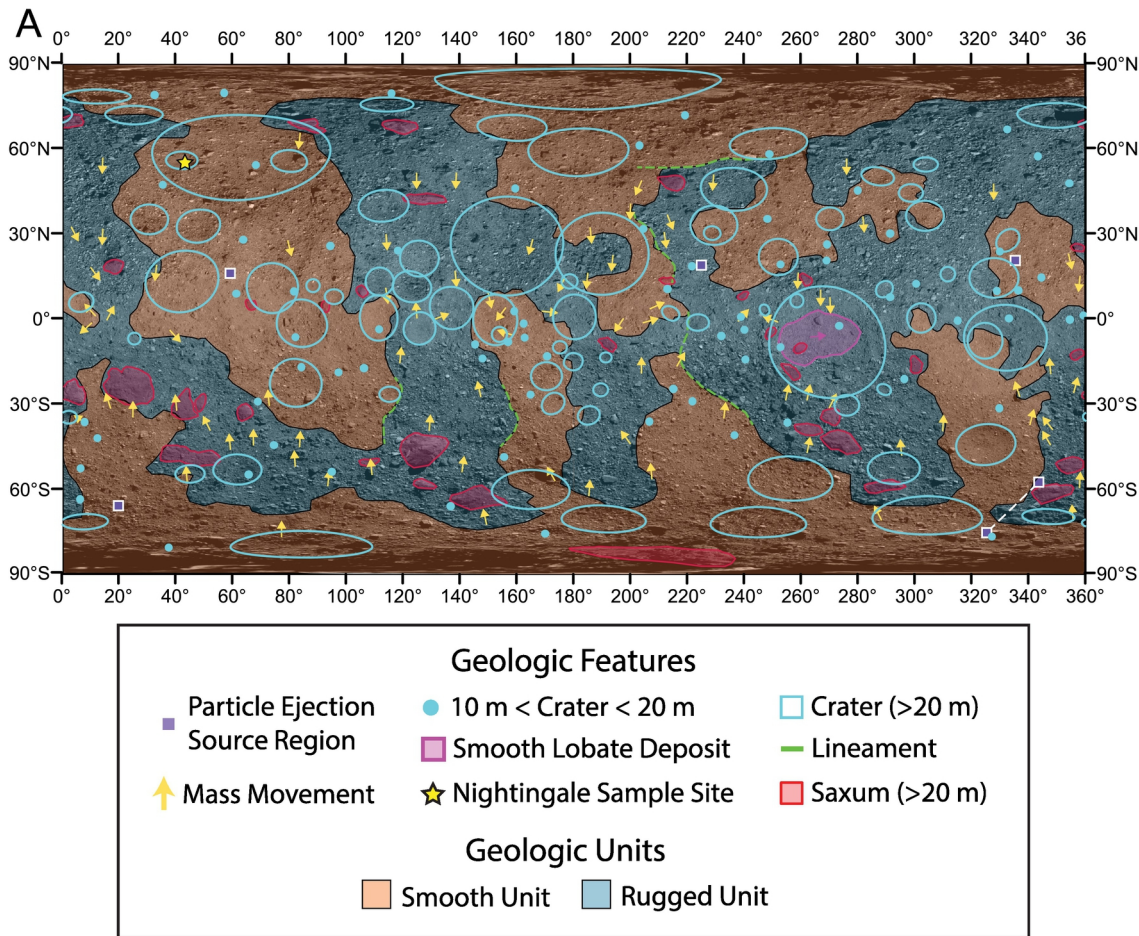
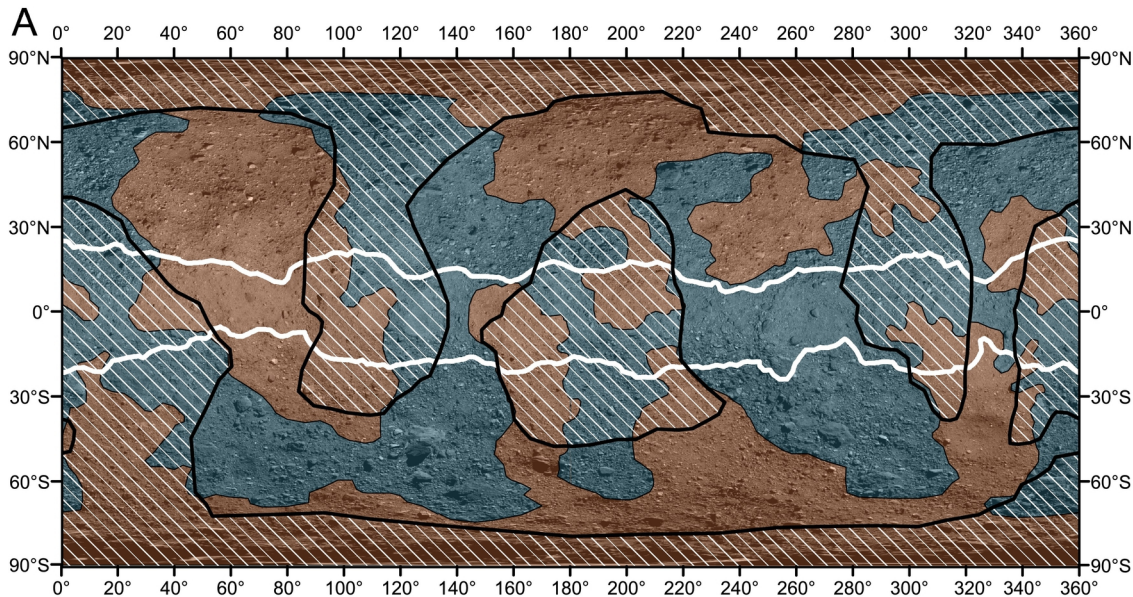


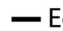



Figure 12



 High-standing region
  Smooth Unit
 Equatorial Bulge
  Rugged Unit

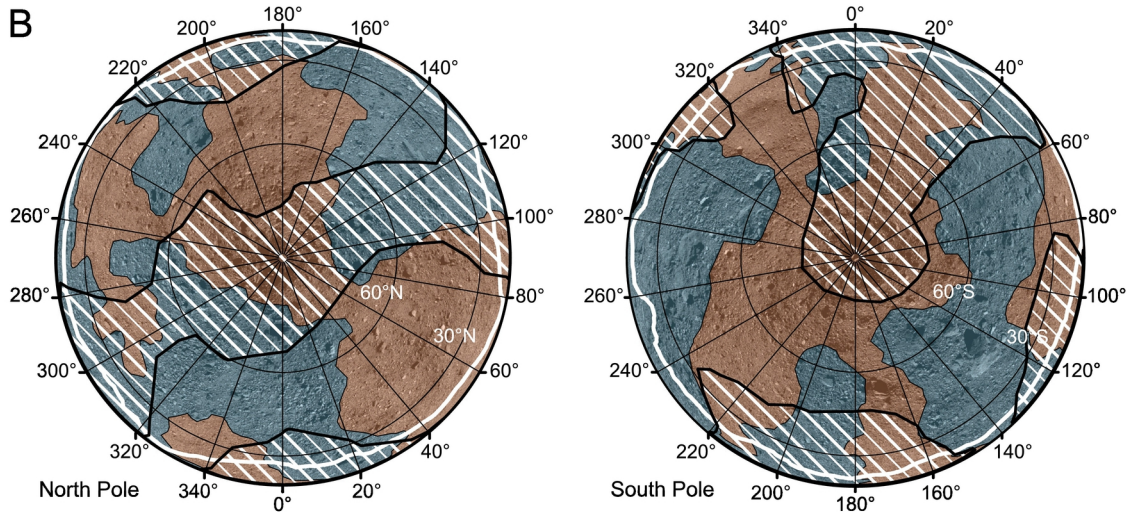


Figure 13

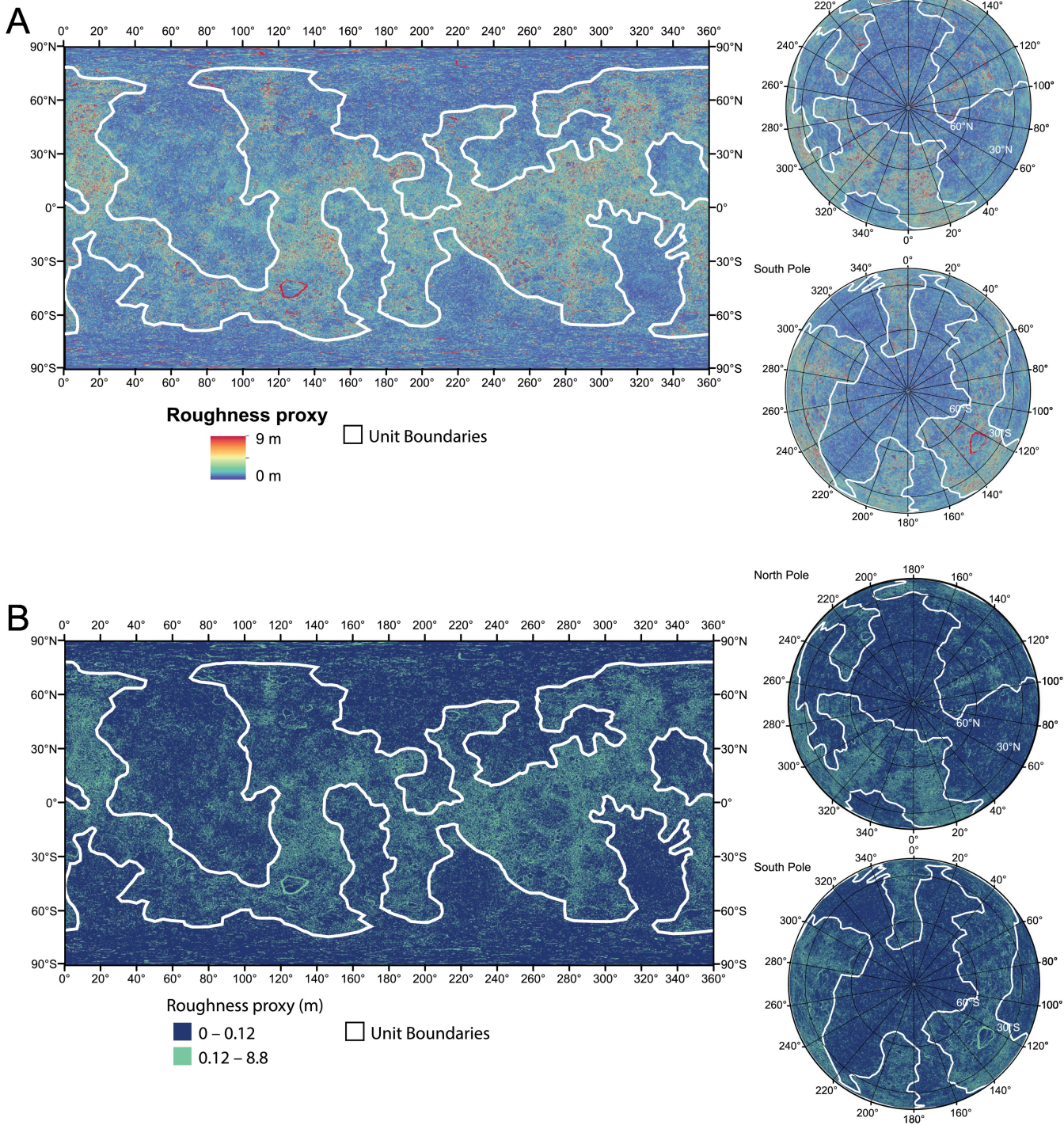


Figure 14

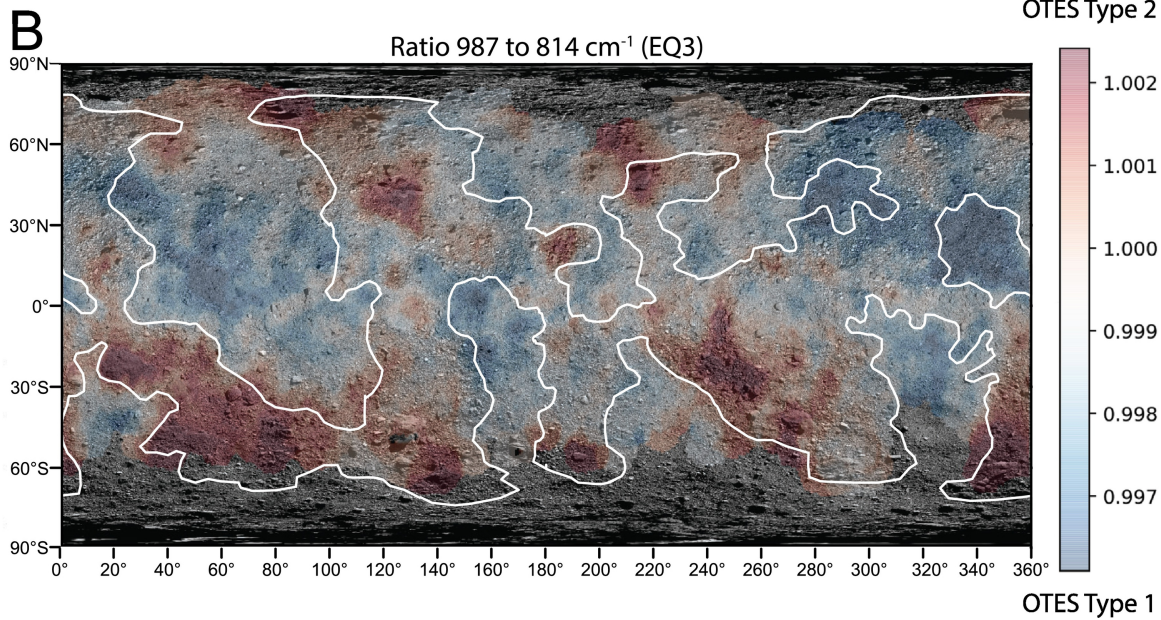
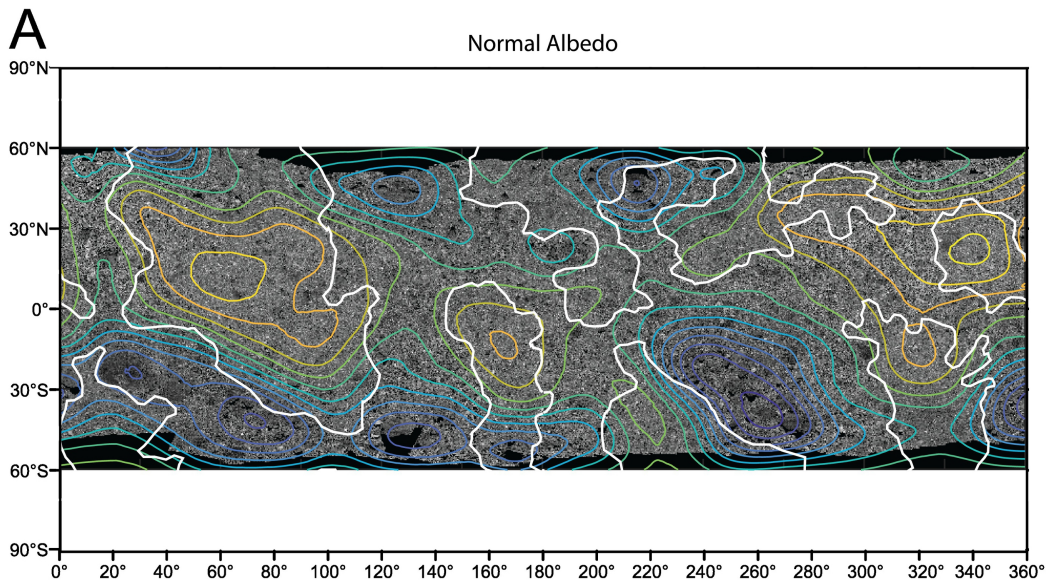


Figure 15

Bennu Global Crater Differential SFD

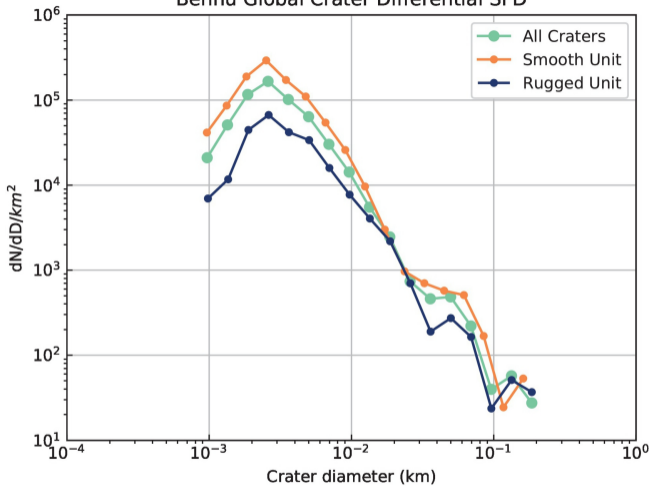


Figure 16

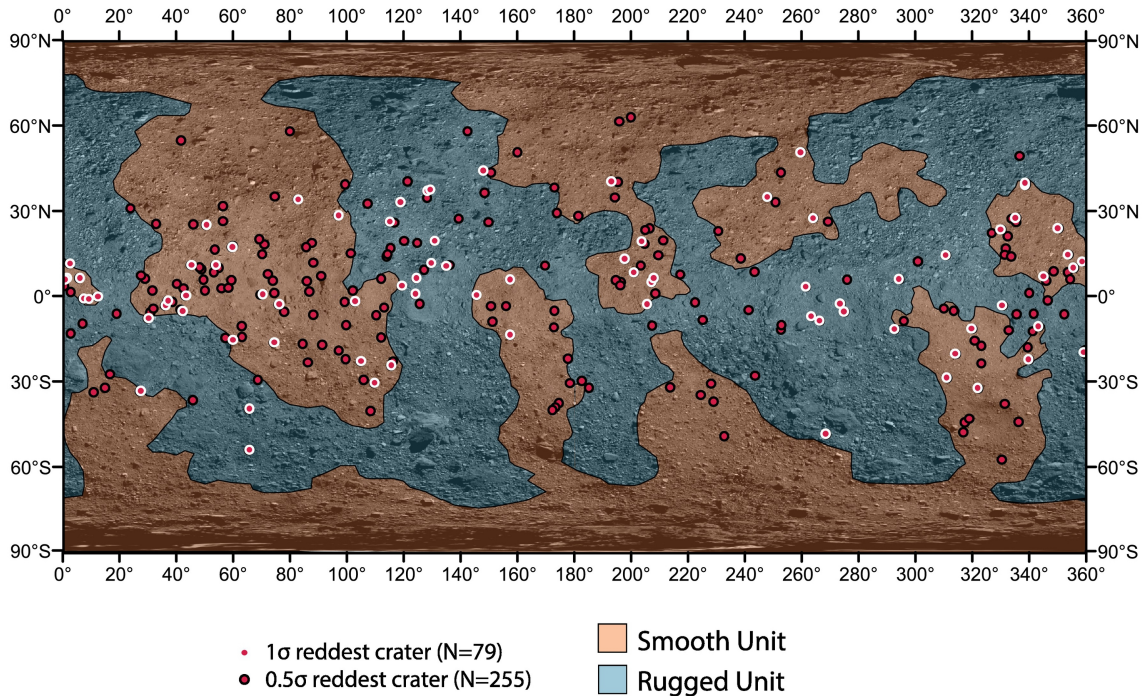


Figure 17

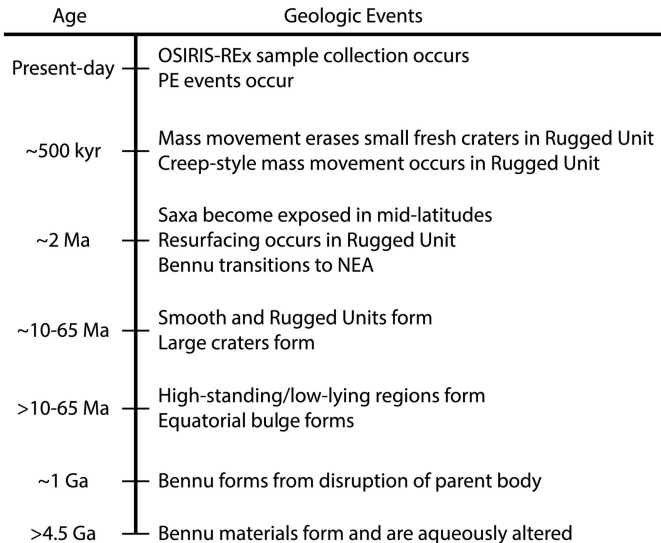


Figure 18